ARTICLE

CD127 imprints functional heterogeneity to diversify monocyte responses in inflammatory diseases

Bin Zhang[1,2]* , Yuan Zhang[1,2]* , Lei Xiong[3] , Yuzhe Li[4] , Yunliang Zhang[1,2] , Jiuliang Zhao[5] , Hui Jiang[5] , Can Li[5] , Yunqi Liu[1,2] , Xindong Liu[6] , Haofei Liu[6] , Yi-Fang Ping[6] , Qiangfeng Cliff Zhang[3,7] , Zheng Zhang[8,9] , Xiu-Wu Bian[6] , Yan Zhao[5] , and Xiaoyu Hu[1,2,7,10]

Inflammatory monocytes are key mediators of acute and chronic inflammation; yet, their functional diversity remains obscure. Single-cell transcriptome analyses of human inflammatory monocytes from COVID-19 and rheumatoid arthritis patients revealed a subset of cells positive for CD127, an IL-7 receptor subunit, and such positivity rendered otherwise inert monocytes responsive to IL-7. Active IL-7 signaling engaged epigenetically coupled, STAT5-coordinated transcriptional programs to restrain inflammatory gene expression, resulting in inverse correlation between CD127 expression and inflammatory phenotypes in a seemingly homogeneous monocyte population. In COVID-19 and rheumatoid arthritis, CD127 marked a subset of monocytes/macrophages that retained hypoinflammatory phenotypes within the highly inflammatory tissue environments. Furthermore, generation of an integrated expression atlas revealed unified features of human inflammatory monocytes across different diseases and different tissues, exemplified by those of the CD127^{high} subset. Overall, we phenotypically and molecularly characterized CD127-imprinted functional heterogeneity of human inflammatory monocytes with direct relevance for inflammatory diseases.

Introduction

Monocytes and macrophages are considered major mediators of inflammation in a plethora of human disease settings, including infectious diseases such as COVID-19 and chronic inflammatory diseases such as rheumatoid arthritis (RA; Donlin et al., 2019; Ermann et al., 2015; Merad and Martin, 2020). During the pathological processes, inflammatory monocytes from the peripheral blood accumulate at the sites of infection and/or inflammation and produce large quantities of proinflammatory mediators, exacerbating disease outcomes by promoting the vicious inflammation cycle (Nathan and Ding, 2010; Shi and Pamer, 2011). Despite the extensive efforts undertaken to understand the ontogeny, functionality, and heterogeneity of inflammatory monocytes (Cormican and Griffin, 2020; Dress et al., 2020; Guilliams et al., 2018), there remain many unanswered

questions, especially pertaining to characterization of in situ monocyte phenotypes in human inflammatory tissues. One question of importance is whether functional characteristics and molecular networks of human inflammatory monocytes could be extrapolated based on the previous observations made with model organisms such as mice (Godec et al., 2016; Hagai et al., 2018; Schroder et al., 2012; Shay et al., 2013). In fact, recent advances in human immunology have begun to unveil unexpected features of human immune cells that could not be predicted based on the existing knowledge largely derived from mouse studies and in vitro cultures (Kuo et al., 2019; Liao et al., 2020; Zhang et al., 2019a). Another outstanding question is whether tissue-infiltrating inflammatory monocytes display distinct properties as a result of tissue adaptation or retain

certain common features regardless of their physical locations. Lack of such understanding would impose significant conceptual and technical barriers to therapeutically targeting human inflammatory diseases (Ermann et al., 2015; van der Poll et al., 2017), a particularly prominent issue amid the COVID-19 pandemic (Vabret et al., 2020), where inflammatory monocytes play a major pathogenic role in lung pathology (Merad and Martin, 2020).

CD127, encoded by the *IL7R* gene, assembles with the *IL2RG*-encoded common γ-chain to form the heterodimeric IL-7 receptor. Upon ligand binding, onset of IL-7 receptor signaling leads to activation of receptor-associated JAK1 and JAK3 and subsequent phosphorylation and nuclear translocation of STAT5 to induce target gene expression. Expression and function of CD127 are best characterized in lymphoid lineage cells. CD127 is predominantly expressed in various stages of lymphoid progenitor cells and in mature lymphocytes, including T cells and innate lymphoid cells (ILCs). Functionally, IL-7 signaling is crucial for development of lymphoid lineages as well as maintenance of immune homeostasis, such as survival of memory T cells (Barata et al., 2019; Leonard et al., 2019). In contrast to lymphocytes, myeloid lineages are not well-recognized CD127-expressing cells (Leonard et al., 2019), albeit that one study documented transient expression of CD127 in mouse fetal monocytes (Leung et al., 2019). While investigating gene expression profiles of human peripheral blood monocytes, earlier studies, including ours, unexpectedly observed highly inducible expression of CD127 upon monocyte activation, typically several hundred–fold over baseline (Hu et al., 2008; Martinez et al., 2006). To our knowledge, these studies represented the initial experimental evidence for CD127 expression in human monocytes, which was confirmed by several subsequent studies (Al-Mossawi et al., 2019; Chen et al., 2013; Kim et al., 2020; Pickens et al., 2011). However, despite the realization of monocytic CD127 expression 15 yr ago, the functional significance and biological outcomes of IL-7 receptor signaling in myeloid cells such as monocytes remain obscure.

Recent technological advancements, especially those at the single-cell level, have enabled description of immune cell phenotypes at an unprecedented resolution (Papalexi and Satija, 2018). Here, we set out to characterize functional and molecular features of CD127^{high} inflammatory monocytes and first found that monocytic expression of CD127 was restricted to humans and was not observed in mice, excluding the possibility of using mice as the model organism and compelling us to investigate these cells in two human inflammatory diseases with high prevalence and significance: COVID-19 and RA. Interrogation of patient samples with multiomics approaches and subsequent mechanistic dissections led to revelation of remarkable functional heterogeneity of human inflammatory monocytes imprinted by the CD127–STAT5 axis. Importantly, advanced bioinformatics analyses integrating multiple data sources unraveled unified features of human inflammatory monocytes, regardless of tissues of origin and disease types, suggesting potentially common monocyte-mediated pathogenic mechanisms in a range of human inflammatory disorders that could serve as new therapeutics targets.

Results

A subset of inflammatory monocytes is strongly CD127 positive in COVID-19 and RA patients

To directly assess expression of CD127 in situ at the sites of infection and/or inflammation, pulmonary autopsy samples from patients succumbing to SARS-CoV-2 infection were analyzed by immunohistochemistry. While minimal CD127 expression was detected in alveoli from individuals who died of noninfectious causes, robust CD127 staining signals were evident in SARS-CoV-2–infected lung tissues and appeared in the regions of CD68 positivity (Fig. 1 A), implying plausible expression of CD127 in monocytes/macrophages. These results were confirmed by co-localization of CD127 and CD68 signals on immunofluorescently stained sections of autopsied COVID-19 lung tissues (Fig. 1 B). Monocyte/macrophage (CD14^{high} CD68^{high}) expression of CD127 was further corroborated at the transcriptome level by single-cell RNA-sequencing (scRNA-seq) analyses of bronchoalveolar lavage fluid (BALF) from nine COVID-19 patients with clinical manifestations ranging from mild (*n* = 3) to severe (*n* = 6; Fig. S1 A). Strikingly, a distinct *IL7R*+ population was revealed to constitute 21% of BALF monocytes/macrophages, and the expression of *IL7R* in monocytes is comparable to that of lymphoid cells (Fig. 1, C–E). Moreover, in contrast to the predicted dominance of *IL7R* positivity by lymphoid cells (Fig. 1 E), the majority (64%) of *IL7R*+ cells in COVID-19 BALF were of the monocyte/macrophage lineage (Fig. 1 F).

To extend the above findings to chronic inflammation, peripheral blood mononuclear cells (PBMCs) from 16 anti-inflammatory treatment–naive RA patients were analyzed for CD127 expression. Compared with the minimal levels of CD127 in CD14+ monocytes from healthy donors, all RA patients examined displayed elevated CD127 expression on blood monocytes at protein and mRNA levels (Fig. 1, G and H). In RA blood monocytes, *IL7R* expression correlated with the expression of a major pathogenic factor, TNF (Fig. 1, H and I; Kalliolias and Ivashkiv, 2016). In addition to circulating monocytes, analyses of synovial immune cell scRNA-seq datasets from 18 RA patients (Zhang et al., 2019a; Fig. S1 B) showed that a distinct population representing nearly 22% of synovial monocytes also exhibited strong *IL7R* positivity at a level comparable to that in T cells (Fig. 1, J–L). Taken together, expression of CD127 on a subset of inflammatory monocytes/macrophages is likely a hallmark of human inflammatory conditions in multiple tissues (infected lungs, peripheral blood, and inflamed joints) and in multiple disease settings (COVID-19 and RA).

Multiple inflammatory stimuli elicit a subset of CD127^{high} human monocytes

To model CD127-expressing human monocytes for facilitation of further mechanistic investigation, we explored the plausible range of inflammatory stimuli capable of inducing this population in human PBMCs and in CD14+ monocytes from healthy blood donors. Stimulation of human PBMCs or CD14+ monocytes with TLR ligands led to a drastic increase of monocytic CD127 at protein and mRNA levels, with the exception of TLR3 agonist polyinosinic:polycytidylic acid (Fig. 2, A and B). Up-regulation of *IL7R* mRNA and protein levels in activated monocytes was
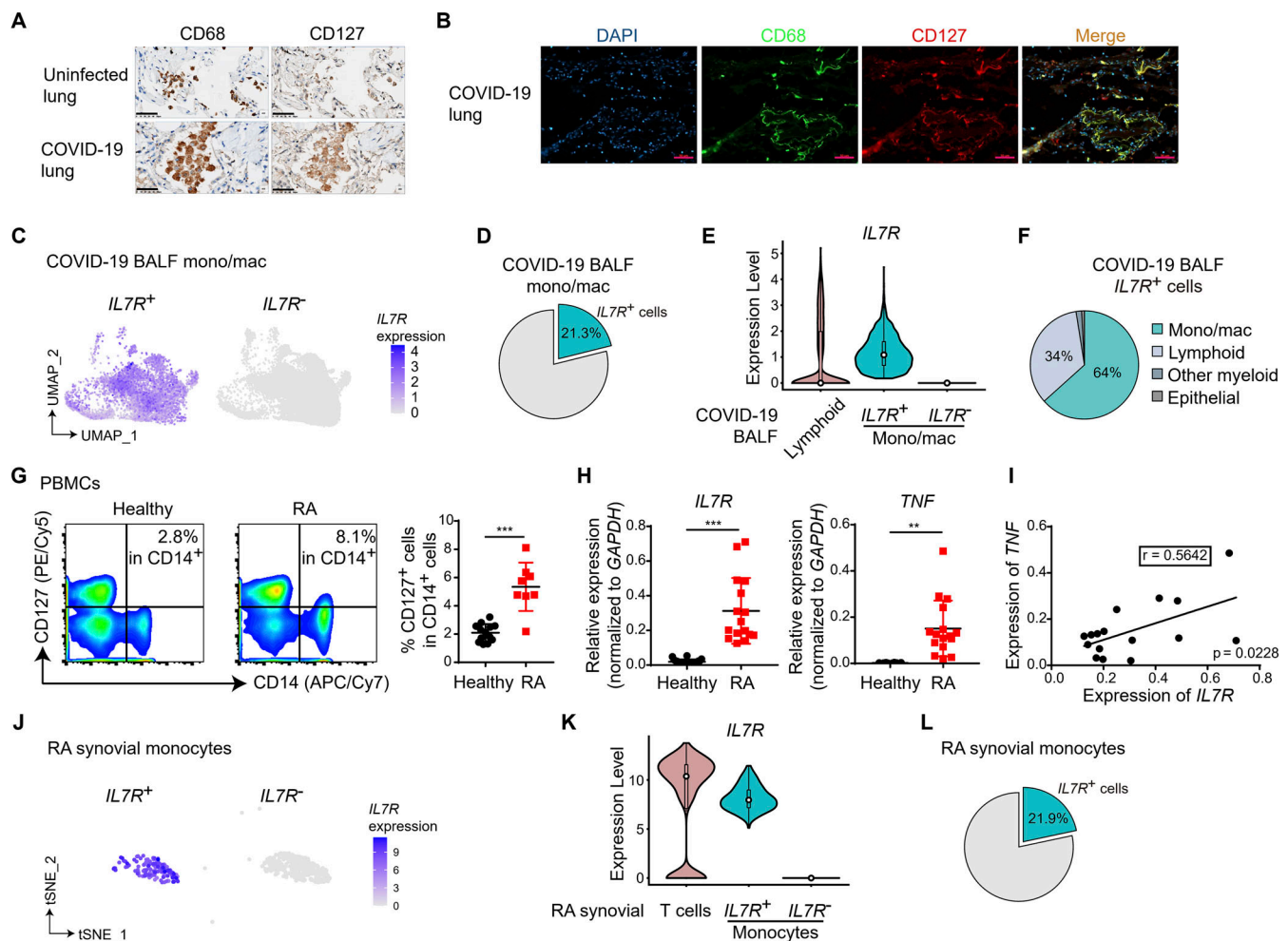
Zhang et al.
CD127 imprints hypoinflammatory human monocytes

Journal of Experimental Medicine   2 of 17
https://doi.org/10.1084/jem.20211191

Figure 1. **CD127^{high} monocytes/macrophages are hallmarks of human inflammatory conditions. (A and B)** Immunohistochemical analysis of CD68 and CD127 expression in lung tissues sections are shown in A. Immunofluorescence staining for DAPI (blue), CD68 (green), and CD127 (red) in sections from COVID-19 lung tissues are shown in B. Uninfected lung tissues and COVID-19 lung tissues were obtained during autopsy as described in Materials and methods. One representative result from tissue sections of three COVID-19 cases is shown. Scale bar, 50 µm. **(C)** UMAP projection of IL7R$^+$ and IL7R$^-$ monocytes/macrophages (mono/mac) in BALF from nine COVID-19 patients (see Materials and methods for details). IL7R expression is shown by the indicated colors. **(D)** Pie graph shows the percentage of IL7R$^+$ cells in COVID-19 BALF mono/mac. **(E)** Violin plot shows the expression levels of IL7R in lymphoid cells and IL7R$^+$ and IL7R$^-$ mono/mac from COVID-19 patient BALF. Each overlaid box indicates the interquartile range with median shown as a circle. **(F)** Pie graph shows the percentages of each cell type in total IL7R$^+$ BALF cells from COVID-19 patients. **(G)** PBMCs were obtained from healthy donors ($n = 13$) and RA patients ($n = 8$), and CD127 expression was measured by FACS analysis. Representative FACS plot (left) and cumulative percentages (right) of CD127$^+$ population in CD14$^+$ monocytes are shown. ***, P < 0.001 by unpaired t test. Data are shown as the mean ± SD. **(H)** In CD14$^+$ monocytes from PBMCs of healthy donors and RA patients, mRNA of IL7R and TNF was measured by qPCR. Relative expression was normalized to internal control (GAPDH). **, P < 0.01; ***, P < 0.001; unpaired t test. Data are shown as the mean ± SD (IL7R, healthy $n = 20$ and RA $n = 16$; TNF, healthy $n = 8$ and RA $n = 16$). **(I)** Linear regression analysis for the expression of TNF and IL7R in CD14$^+$ monocytes from each RA patient in H. Correlation coefficient r and P value by F-test are labeled. **(J)** t-Distributed stochastic neighbor embedding (tSNE) projection of IL7R$^+$ and IL7R$^-$ cells in RA synovial monocytes (see Materials and methods for details). IL7R expression is shown by the indicated colors. **(K)** Violin plot shows the expression levels of IL7R in T cells and IL7R$^+$ and IL7R$^-$ monocytes in RA synovial tissues. Each overlaid box indicates the interquartile range with median shown as a circle. **(L)** Pie graph shows the percentage of IL7R$^+$ cells in RA synovial monocytes. Each data point in G–I represents one individual donor or patient.

consistently observed in >20 healthy donors examined, with the cell surface expression peaking ~6 h after activation (Fig. 2, C–F). Inducible CD127 expression was comparable to that of the constitutive CD127 in T cells (Fig. S2 A) and dependent on canonical TLR signaling modules such as NF-κB and MAPKs as evidenced by pharmaceutical inhibition and RNA interference (Fig. S2, B–E). Activation-induced CD127 up-regulation was observed in all three subsets of human blood monocytes defined by binary expression of CD14 and CD16 (Fig. 2 G and Fig. S2, F–H),

suggesting that CD127 up-regulation is a common feature of human monocyte activation. In addition to pathogen-associated molecular patterns that might contribute to the appearance of CD127$^+$ monocytes in infectious diseases, we also sought such factors in the context of sterile inflammation and pursued TNF as a plausible candidate because its levels correlated with CD127 expression in RA blood monocytes (Fig. 1 I). TNF treatment consistently up-regulated CD127 in monocytes from healthy donors, albeit to a lesser extent than LPS (Fig. 2, H and I).
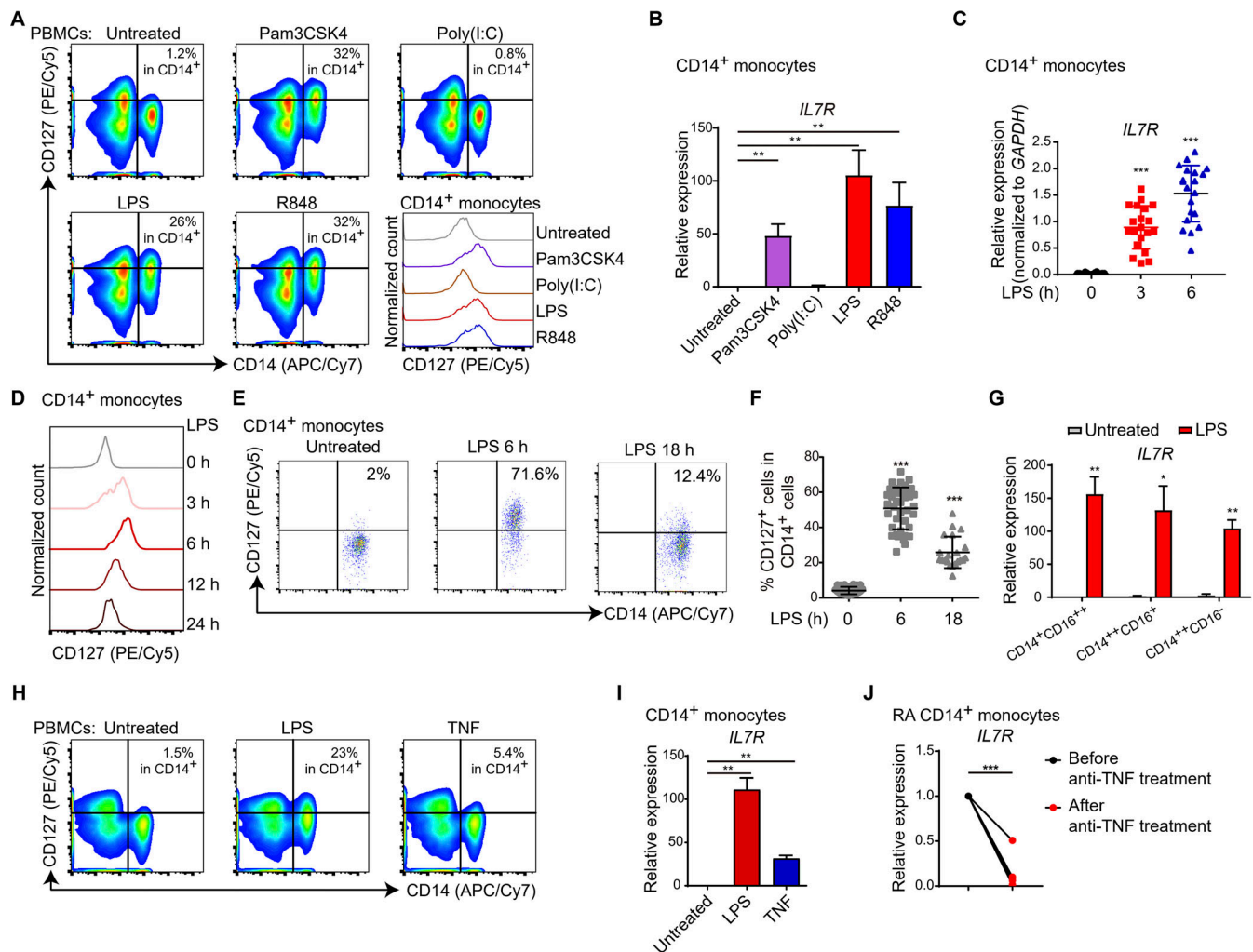
Figure 2. **CD127^{high} monocytes are inducible by exogenous and endogenous inflammatory stimuli. (A and B)** Cells obtained from healthy blood donors were stimulated with Pam3CSK4 (100 ng/ml), polyinosinic:polycytidylic acid (Poly(I:C); 1 µg/ml), LPS (10 ng/ml), or R848 (1 µg/ml) as indicated. CD127 expression in PBMCs with 6-h stimulation was measured by FACS. One representative FACS result from three independent experiments is shown (A), and histograms in A show the CD127 staining signal in CD14^{+} cells under each indicated condition. In CD14^{+} monocytes from healthy donor PBMCs upon 3-h stimulation, mRNA of *IL7R* was measured by qPCR (B). Relative expression was normalized to internal control (*GAPDH*) and expressed relative to untreated sample. **, P < 0.01 by paired *t* test. Data are shown as the mean ± SD of four independent experiments. **(C)** CD14^{+} monocytes were treated with 10 ng/ml LPS for 3 h and 6 h, and mRNA of *IL7R* was measured by qPCR. Relative expression was normalized to internal control (*GAPDH*). ***, P < 0.001 by unpaired *t* test. Data are shown as the mean ± SD of 20 independent experiments. **(D)** Analysis of CD127 expression by FACS in CD14^{+} monocytes during the time course of LPS stimulation (10 ng/ml) as indicated. **(E and F)** CD14^{+} monocytes were treated with or without 10 ng/ml LPS for the indicated time points, and CD127 expression was measured by FACS. Representative FACS distribution (E) and cumulative percentage (F) are shown. ***, P < 0.001 represents comparison of LPS-stimulated samples with unstimulated samples by unpaired *t* test. Data are shown as the mean ± SD of multiple independent experiments. LPS 0 h, n = 39; LPS 6 h, n = 39; LPS 18 h, n = 21. **(G)** Three monocyte subsets were FACS sorted from PBMCs as shown in Fig. S2 F and then were treated with or without 10 ng/ml LPS for 3 h. *IL7R* expression was measured by qPCR. Relative expression was normalized to internal control (*GAPDH*) and expressed relative to LPS-untreated CD14^{+}CD16^{++} sample. **, P < 0.01; *, P < 0.05; unpaired *t* test. Data are shown as the mean ± SD of three independent experiments. **(H and I)** PBMCs from healthy donors were treated with LPS (10 ng/ml) or human TNF (100 ng/ml). Upon 6-h LPS or TNF treatment, CD127 expression was measured by FACS. Representative FACS distribution is shown (H). mRNA of *IL7R* was measured in 3-h LPS- or TNF-treated CD14^{+} monocytes by qPCR (I). Relative expression was normalized to internal control (*GAPDH*) and expressed relative to untreated sample. **, P < 0.01 by paired *t* test. Data in I are shown as the mean ± SD of three independent experiments. **(J)** mRNA level of *IL7R* was measured by qPCR in monocytes from RA patients (n = 5) before and after etanercept anti-TNF treatment for 2 mo. Relative expression was normalized to internal control (*GAPDH*), expressed relative to before treatment sample, and shown as the paired data points for before and after treatment samples in each patient. ***, P < 0.001 by paired *t* test. Independent experiments in A–I were performed with cells from one healthy donor for each experiment.

Importantly, clinically applied TNF blockade treatment significantly reduced *IL7R* expression in RA monocytes (Fig. 2 J), further solidifying a role for TNF in up-regulation of CD127 in vivo.

Because mice are widely used as model organisms to mimic human immunological processes, we assessed whether human

monocytic expression of CD127 could be recapitulated in mice. As expected, mouse blood monocytes and tissue-resident macrophages did not express CD127 at homeostasis (Yoshida et al., 2019; Fig. S2 I). However, in contrast to the observations in humans, LPS stimulation up to 18 h failed to induce CD127 in

murine blood CD11b+ monocytes and various macrophage populations examined (Fig. S2, J and K; and data not shown). Consistent with the lack of expression in vitro, in models of pulmonary inflammation (Sajti et al., 2020), CD127 remained undetectable in pulmonary myeloid cells, including alveolar macrophages, interstitial macrophages, and resident monocytes (Fig. S2 L). Taken together, pathogen-associated molecular patterns and sterile inflammatory stimulation elicit a subset of CD127-expressing monocytes in humans but not in mice, highlighting the unique features of human inflammatory monocytes and mandating the necessity to conduct the following experiments in a human system.

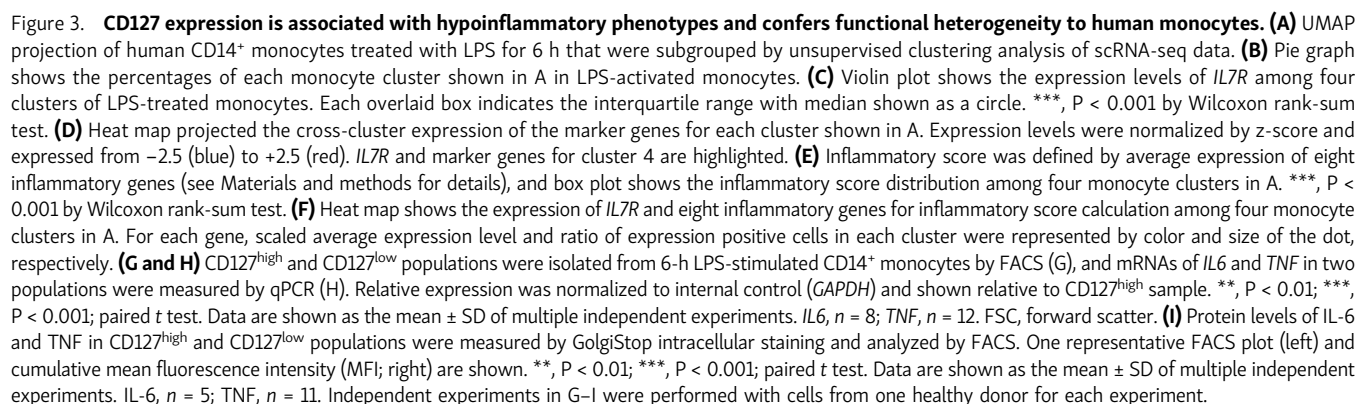## CD127 imposes functional heterogeneity in activated monocytes

Given the wide range of CD127 expression among activated human monocytes (Fig. 2, E and F), we hypothesized that CD127 levels may correlate with certain monocyte phenotypes and subjected LPS-activated human CD14+ monocytes to scRNA-seq to reveal the potential diversities. Unsupervised clustering revealed four groups of cells within seemingly uniformly activated monocytes (Fig. 3, A and B). Interestingly, *IL7R* expression was highest in cluster 1 and exhibited a decreasing gradient from cluster 1 to cluster 4 (Fig. 3 C). In fact, *IL7R* is one of the top 15 signature genes of cluster 1, whereas cluster 4 was enriched with a number of well-defined proinflammatory mediators (Fig. 3 D). To further quantitatively assess the inflammatory phenotypes of these cells, we devised a numeric index "inflammatory score" based on an algorithm (Stuart et al., 2019) reflecting expression levels of eight prototypical inflammatory genes (see Materials and methods for details). Inflammatory score inversely correlated with the expression of *IL7R*, with the highest inflammatory score shown for cluster 4, which exhibited the lowest level of *IL7R* (Fig. 3 E). Such a trend could also be clearly visualized for individual inflammatory genes (Fig. 3 F). To validate the differences of inflammatory responses observed from single-cell analyses, we sorted CD127high and CD127low LPS-activated monocytes (Fig. 3 G). Consistent with the results from the single-cell analyses, CD127low monocytes produced significantly higher levels of inflammatory mediators IL-6 and TNF than their CD127high counterparts (Fig. 3, H and I). In contrast to divergent inflammatory phenotypes, certain effector functions, such as NO production and phagocytosis capacity, remained comparable between CD127high and CD127low monocyte populations (Fig. S3, A and B), suggesting relative functional specificity regarding CD127-delineated heterogeneity of inflammatory phenotypes. Together, these results implied that, within a highly defined system consisting of purified monocytes and a single stimulus, human monocytes displayed a diverse spectrum of inflammatory responses whose strengths were inversely correlated with CD127 expression.

CD127 up-regulation renders monocytes hypersensitive to IL-7 and engages a STAT5-mediated feedback loop to dampen inflammation

Next, we wished to investigate the mechanisms by which CD127 modulated monocyte phenotypes. In human monocytes, another

subunit of IL-7 receptor, the *IL2RG*-encoded common γ-chain, was constitutively expressed (Fig. S3 C). Therefore, we speculated that induction of CD127 would render activated human monocytes responsive to IL-7 that is otherwise inert for resting monocytes. Indeed, resting monocytes did not respond to stimulation with up to 10 ng/ml of IL-7 as measured by STAT5 tyrosine phosphorylation (Fig. 4 A). Interestingly, activated monocytes exhibited high sensitivity to IL-7 as shown by induction of STAT5 activation with a picogram range of the cytokine (Fig. 4 A), comparable to the concentrations of IL-7 detected in the in vitro monocyte culture system (Fig. S3 D). With IL-7 signaling in human T cells serving as a positive control (Fig. S3 E), the above data implied that activated human monocytes were competent to sense IL-7 via CD127-mediated IL-7 receptor signaling. Next, to assess whether active receptor signaling was causally related to the hypoinflammatory phenotypes, we knocked down CD127 expression by transfecting *IL7R*-targeting siRNA into CD14+ human monocytes (Fig. 4 B). Compared with control siRNA-transfected monocytes, knocking down *IL7R* resulted in significantly up-regulated *IL6* and *TNF* mRNA in activated monocytes (Fig. 4 B). Moreover, addition of exogenous IL-7 to activated monocytes suppressed *IL6* expression (Fig. S3, F and G), further supporting a negative role of monocytic IL-7 receptor signaling in inflammatory gene expression.

To comprehensively characterize features of CD127-imposed heterogeneity, we profiled the chromatin accessibility landscapes of sorted CD127high and CD127low human monocytes by assay for transposase-accessible chromatin coupled with high-throughput sequencing (ATAC-seq; Fig. 4 C). Analyses of ATAC-seq data obtained from three individual donors consistently revealed open chromatin regions (OCRs) that were differentially enriched in CD127high versus CD127low populations, thus termed "CD127high feature OCRs" and "CD127low feature OCRs," respectively (Fig. 4, D–F). In further epigenetic characterizations, CD127low feature OCRs implicated gene-proximal epigenetic features (Fig. S4 A), which were exemplified by the permissive chromatin regions around the transcription start site (TSS) of inflammatory marker genes of cluster 4 in scRNA-seq analyses of activated monocytes (Fig. S4, B–D). CD127high feature OCRs were marked by H3K4me1 and H3K27ac, implicating intergenic enhancer-like features (Fig. S4, E and F). Intriguingly, CD127high feature OCRs displayed permissive states in the resting state, and their accessibility was not further increased by LPS-mediated activation (Fig. S4, G and H), implying potentially stable epigenetic characters. Furthermore, unbiased motif analysis identified STAT5 as the most significantly enriched transcriptional module in CD127high feature OCRs (Fig. 4 G), suggesting that STAT5 is the likely effector transcription factor that mediates the anti-inflammatory effects of CD127 in human monocytes. Indeed, in line with the observation of *IL7R* knockdown experiments, inhibiting STAT5 activation in human monocytes by a STAT5 inhibitor resulted in enhanced *IL6* and *TNF* expression (Fig. 4 H). Taken together, CD127 up-regulation conferred activated human monocyte responsiveness to IL-7 and imposed a STAT5-coordinated transcriptional program to restrain inflammation.

Zhang et al.
CD127 imprints hypoinflammatory human monocytes

Journal of Experimental Medicine   5 of 17
https://doi.org/10.1084/jem.20211191

Figure 3. **CD127 expression is associated with hypoinflammatory phenotypes and confers functional heterogeneity to human monocytes. (A)** UMAP projection of human CD14+ monocytes treated with LPS for 6 h that were subgrouped by unsupervised clustering analysis of scRNA-seq data. **(B)** Pie graph shows the percentages of each monocyte cluster shown in A in LPS-activated monocytes. **(C)** Violin plot shows the expression levels of *IL7R* among four clusters of LPS-treated monocytes. Each overlaid box indicates the interquartile range with median shown as a circle. ***, P < 0.001 by Wilcoxon rank-sum test. **(D)** Heat map projected the cross-cluster expression of the marker genes for each cluster shown in A. Expression levels were normalized by z-score and expressed from −2.5 (blue) to +2.5 (red). *IL7R* and marker genes for cluster 4 are highlighted. **(E)** Inflammatory score was defined by average expression of eight inflammatory genes (see Materials and methods for details), and box plot shows the inflammatory score distribution among four monocyte clusters in A. ***, P < 0.001 by Wilcoxon rank-sum test. **(F)** Heat map shows the expression of *IL7R* and eight inflammatory genes for inflammatory score calculation among four monocyte clusters in A. For each gene, scaled average expression level and ratio of expression positive cells in each cluster were represented by color and size of the dot, respectively. **(G and H)** CD127high and CD127low populations were isolated from 6-h LPS-stimulated CD14+ monocytes by FACS (G), and mRNAs of *IL6* and *TNF* in two populations were measured by qPCR (H). Relative expression was normalized to internal control (*GAPDH*) and shown relative to CD127high sample. **, P < 0.01; ***, P < 0.001; paired *t* test. Data are shown as the mean ± SD of multiple independent experiments. *IL6*, n = 8; *TNF*, n = 12. FSC, forward scatter. **(I)** Protein levels of IL-6 and TNF in CD127high and CD127low populations were measured by GolgiStop intracellular staining and analyzed by FACS. One representative FACS plot (left) and cumulative mean fluorescence intensity (MFI; right) are shown. **, P < 0.01; ***, P < 0.001; paired *t* test. Data are shown as the mean ± SD of multiple independent experiments. IL-6, n = 5; TNF, n = 11. Independent experiments in G–I were performed with cells from one healthy donor for each experiment.

CD127high monocytes are featured by STAT5–c-Maf–centric chromatin landscape

To elucidate the mechanisms underlying CD127-STAT5–mediated effects, CD127high and CD127low populations were profiled by RNA-seq (Fig. 5 A), revealing that *MAF*-encoded c-Maf, an established anti-inflammatory transcription factor (Locati et al., 2020; Fig. S4, I and J), was enriched in CD127high monocytes relative to CD127low cells (Fig. 5 B). Moreover, analyses of human monocyte c-Maf chromatin immunoprecipitation followed by sequencing (ChIP-seq) datasets (Kang et al., 2017) unraveled preferential deposition of c-Maf in CD127high feature OCRs with minimal occupancy in CD127low feature OCRs (Fig. 5, C and D), implying that CD127high monocytes were characterized by a c-Maf–imposed transcriptional signature. Furthermore, *MAF* was a direct STAT5 target gene in human monocytes evidenced by binding of STAT5 to a putative IFN-γ activation site (GAS) in the promoter region (Fig. 5

E). Importantly, STAT5 inhibition consistently led to down-regulation of *MAF* in activated monocytes (Fig. 5 F), supporting a positive role for STAT5 in tuning *MAF* expression. To gain better understanding of STAT5 functionality, we profiled global STAT5 occupancy in CD127high monocytes by ChIP-seq (Fig. 5, G and H). In monocytes, STAT5 predominantly bound to intergenic regions (Fig. 5 I), reminiscent of the intergenic enhancer-like CD127high feature OCRs (Fig. S4, A and B). Indeed, STAT5 occupancy exhibited a strong preference toward CD127high feature OCRs relative to CD127low feature OCRs (Fig. 5, J–M), suggesting that STAT5-associated epigenetic features were among the defining characteristics of CD127high monocytes. Together, the above results implied that the CD127–STAT5 axis exploited the "M2" gene, *MAF*, to exert anti-inflammatory effects that contributed to the functional heterogeneity in human inflammatory monocytes.
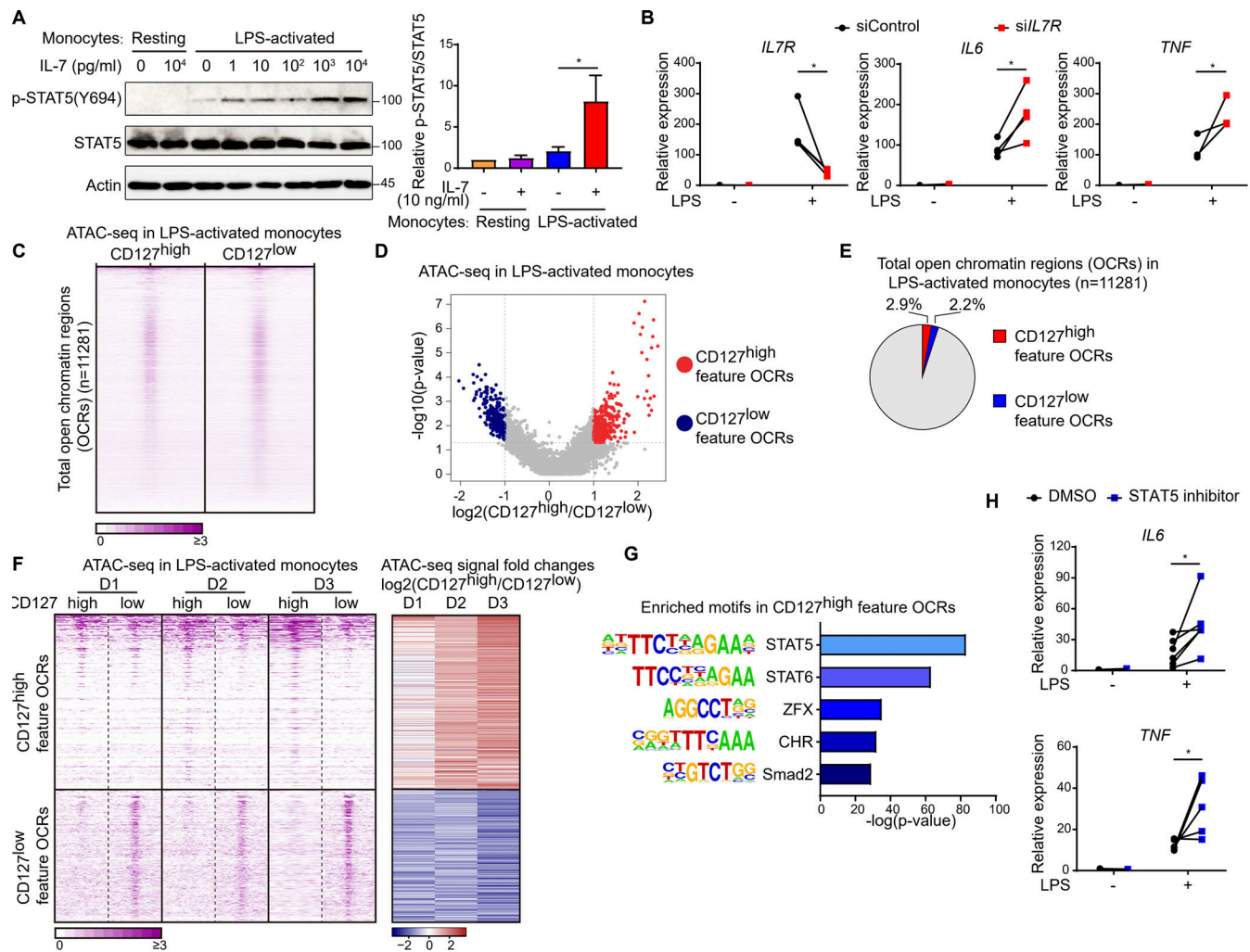
Figure 4. **CD127–STAT5 axis constrains inflammatory gene expression in human monocytes. (A)** CD14^{+} monocytes were pretreated with or without LPS for 6 h, followed by various doses of human IL-7 (from 1 pg/ml to 10 ng/ml) for 30 min. STAT5 activation was detected by Western blotting. β-Actin was used as a loading control. One representative result from three independent experiments is shown (left). The protein level of p-STAT5(Y694) was quantified by densitometry, normalized to total STAT5 protein, and expressed relative to untreated (without LPS and IL-7) sample (right). *, P < 0.05; paired t test. Data are shown as the mean ± SD of three independent experiments. **(B)** CD14^{+} monocytes were transfected with negative control or IL7R-specific siRNA (siControl or siIL7R). 2 d after transfection, cells were stimulated with LPS (10 ng/ml) for 3 h, and mRNA of IL7R, IL6, and TNF were measured by qPCR. Relative expression was normalized to an internal control (GAPDH) and expressed relative to LPS untreated siControl sample. *, P < 0.05; paired t test. Each pair of data points indicates an independent experiment. IL7R, n = 4; IL6, n = 4; TNF, n = 3. **(C)** With CD127-based FACS sorting for 6-h LPS-treated monocytes, ATAC-seq datasets were generated for CD127^{high} and C127^{low} monocytes from three donors separately. Heat maps of pooled ATAC-seq signals around the total identified OCRs were shown in CD127^{high} and C127^{low} monocytes. Each row indicates one OCR, and the rows were sorted by the decreasing ATAC-seq signals in OCRs. **(D)** Volcano plot shows the differentially opened OCRs by ATAC-seq between CD127^{high} and CD127^{low} monocytes (P < 0.05; fold change ≥2 or ≤0.5). Highly opened OCRs in CD127^{high} population (CD127^{high} feature OCRs) and highly opened OCRs in CD127^{low} population (CD127^{low} feature OCRs) are indicated in red and in blue, respectively. Fold changes are shown as the mean value of CD127^{high}/CD127^{low} ratio from three donors. **(E)** Pie graph shows the percentages of CD127^{high} and C127^{low} feature OCRs in total identified OCRs in LPS-activated monocytes. **(F)** Heat maps (left) show the ATAC-seq signals around the CD127^{high} feature and CD127^{low} feature OCRs in each pair of CD127^{high} and CD127^{low} monocytes from three donors and corresponding ATAC-seq signal fold changes (CD127^{high}/CD127^{low}; right) were log₂ transformed and expressed by color from blue (negative) to red (positive). **(G)** Top five results from motif enrichment analysis in CD127^{high} monocyte featured OCRs are shown according to the decreasing –log₁₀(P value) for enriched motifs. P value by binomial distribution. **(H)** CD14^{+} monocytes were pretreated with STAT5 inhibitor (100 μM) for 2 h and then were stimulated with LPS (10 ng/ml). mRNA levels of IL6 (LPS 6 h) and TNF (LPS 3 h) were measured using qPCR. *, P < 0.05 by paired t test. Each pair of data points represents an independent experiment (n = 6). Independent experiments in A, B, and H were performed with cells from one healthy donor for each experiment.

Unified monocyte phenotypes in human inflammatory conditions

Upon characterization of CD127-imposed monocyte functional heterogeneity in vitro, we next wished to validate these findings in vivo in human disease settings. Profiling synovial monocytes (Fig. S1 B) and peripheral blood monocytes (Fig. S5, A and B)

from RA patients with scRNA-seq revealed that IL7R^{+} cells were largely nonoverlapping with the highly inflammatory counterparts and displayed minimal inflammatory features quantitated by inflammatory score and exemplified by expression of representative inflammatory genes (Fig. 6, A and B). Similarly, in COVID-19 BALF monocytes/macrophages, the IL7R^{+} population
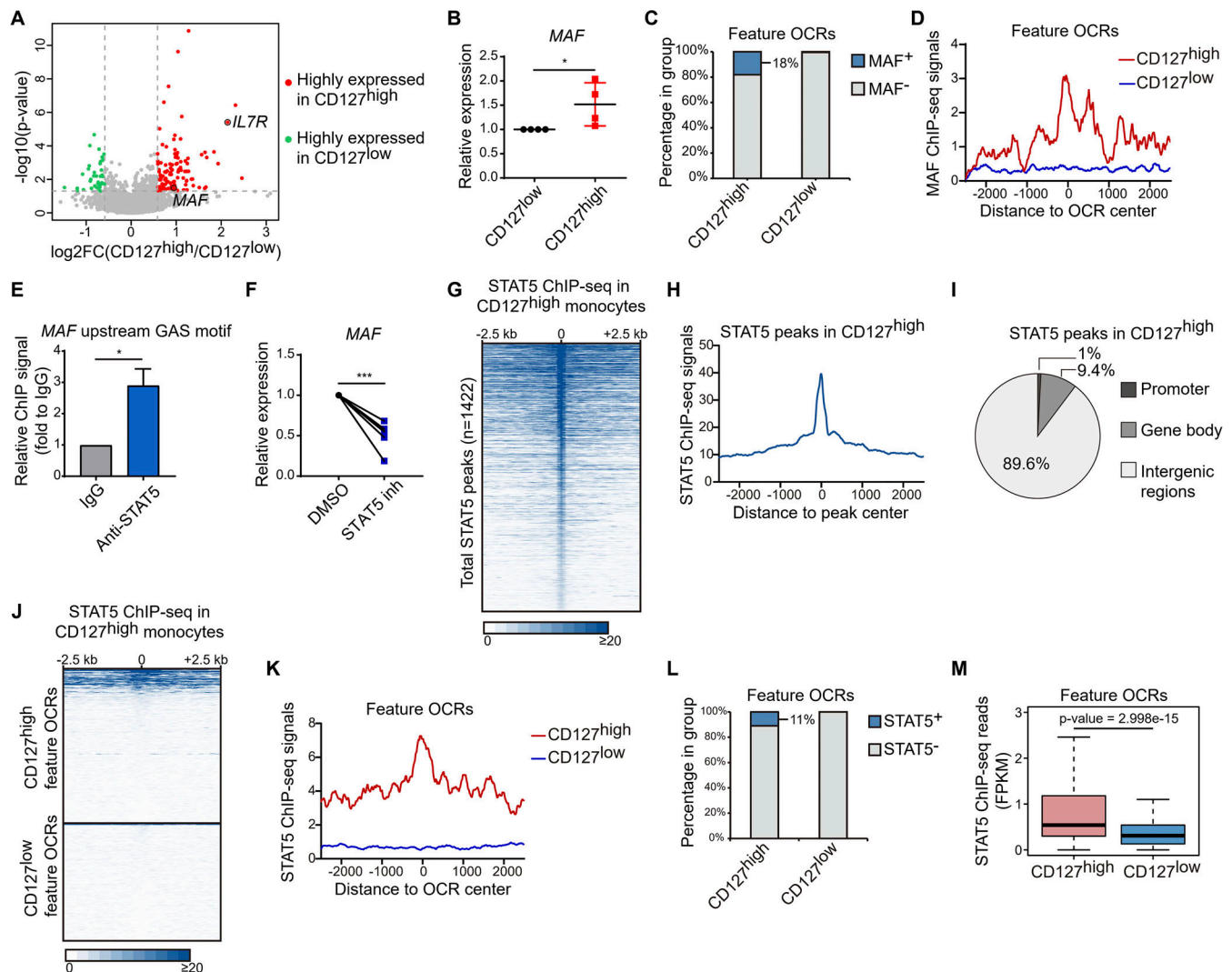
Zhang et al.
CD127 imprints hypoinflammatory human monocytes

Journal of Experimental Medicine   7 of 17
https://doi.org/10.1084/jem.20211191

Figure 5. **STAT5 reinforces unique epigenetic landscape in CD127high monocytes to impose hypoinflammatory phenotype. (A)** RNA-seq separately performed in CD127high and CD127low populations from LPS 6-h stimulated CD14+ monocytes of three healthy donors. Volcano plot shows the significant differential expression between CD127high and CD127low populations (P < 0.05; fold change ≥1.5 or ≤0.67). Highly expressed genes in CD127high population and CD127low population are colored in red and in green, respectively. Two CD127high highly expressed genes, IL7R and MAF, were labeled. Fold changes (FCs) are shown as mean value of CD127high/CD127low ratio from three donors. **(B)** mRNA of MAF in CD127high and CD127low populations from LPS 6-h stimulated CD14+ monocytes was measured by qPCR. Relative expression was normalized to internal control (GAPDH) and expressed relative to CD127low sample. *, P < 0.05 by paired t test. Data are shown as the mean ± SD of four independent experiments. **(C)** Cumulative percentage plot shows the portions of CD127high and CD127low feature OCRs with significant MAF enrichment (MAF+) in resting human monocytes. **(D)** Average MAF ChIP-seq signals in resting human monocytes are shown around the CD127high and CD127low feature OCRs. **(E)** The occupancy of STAT5 in the MAF upstream GAS motif was assessed by ChIP-qPCR in LPS 6-h stimulated THP-1 cells. Relative STAT5 ChIP signals were expressed relative to IgG ChIP negative control sample. *, P < 0.05 by paired t test. Data are shown as the mean ± SD of three independent experiments. **(F)** CD14+ monocytes were pretreated with STAT5 inhibitor (100 μM) for 2 h and then were stimulated with LPS (10 ng/ml) for 6 h. mRNA of MAF was measured by qPCR. Relative expression is normalized to internal control (GAPDH) and expressed relative to DMSO-treated sample. ***, P < 0.001 by paired t test. Results from six independent experiments are shown. **(G)** Heat map showing the STAT5 ChIP-seq signals around each identified STAT5 peak in CD127high monocytes by each row. The rows were sorted by decreasing STAT5 ChIP-seq signals in peak regions. **(H)** Average STAT5 ChIP-seq signals in CD127high monocytes are shown around total STAT5 peak regions. **(I)** Pie graph shows the genomic distribution of STAT5 peaks in CD127high monocytes. **(J)** Heat map shows the STAT5 ChIP-seq signals in CD127high monocytes around the CD127high and CD127low feature OCRs. **(K)** Average STAT5 ChIP-seq signals in CD127high monocytes are shown around the CD127high and CD127low feature OCRs. **(L)** Cumulative percentage plot showing the portions of CD127high and CD127low feature OCRs with significant STAT5 enrichment (STAT5+) in CD127high monocytes. **(M)** STAT5 ChIP-seq signals in CD127high and CD127low feature OCRs were counted as FPKM and are shown as a box plot. P value was derived by Wilcoxon rank-sum test. Independent experiments in B and D were performed with cells from one healthy donor for each experiment.

also did not largely overlap with the highly inflammatory cells and exhibited minimal inflammatory properties (Fig. 6, C and D). Importantly, disease severity inversely correlated with IL7R expression in COVID-19 patients (Fig. 6 E). In mild

COVID-19 patients, on average, 44% of BALF monocytes/macrophages were IL7R+ cells; yet, this percentage was 18% in severe COVID-19 patients (Fig. 6 F and Fig. S5 C). The differential IL7R patterns in monocytes were not due to the global
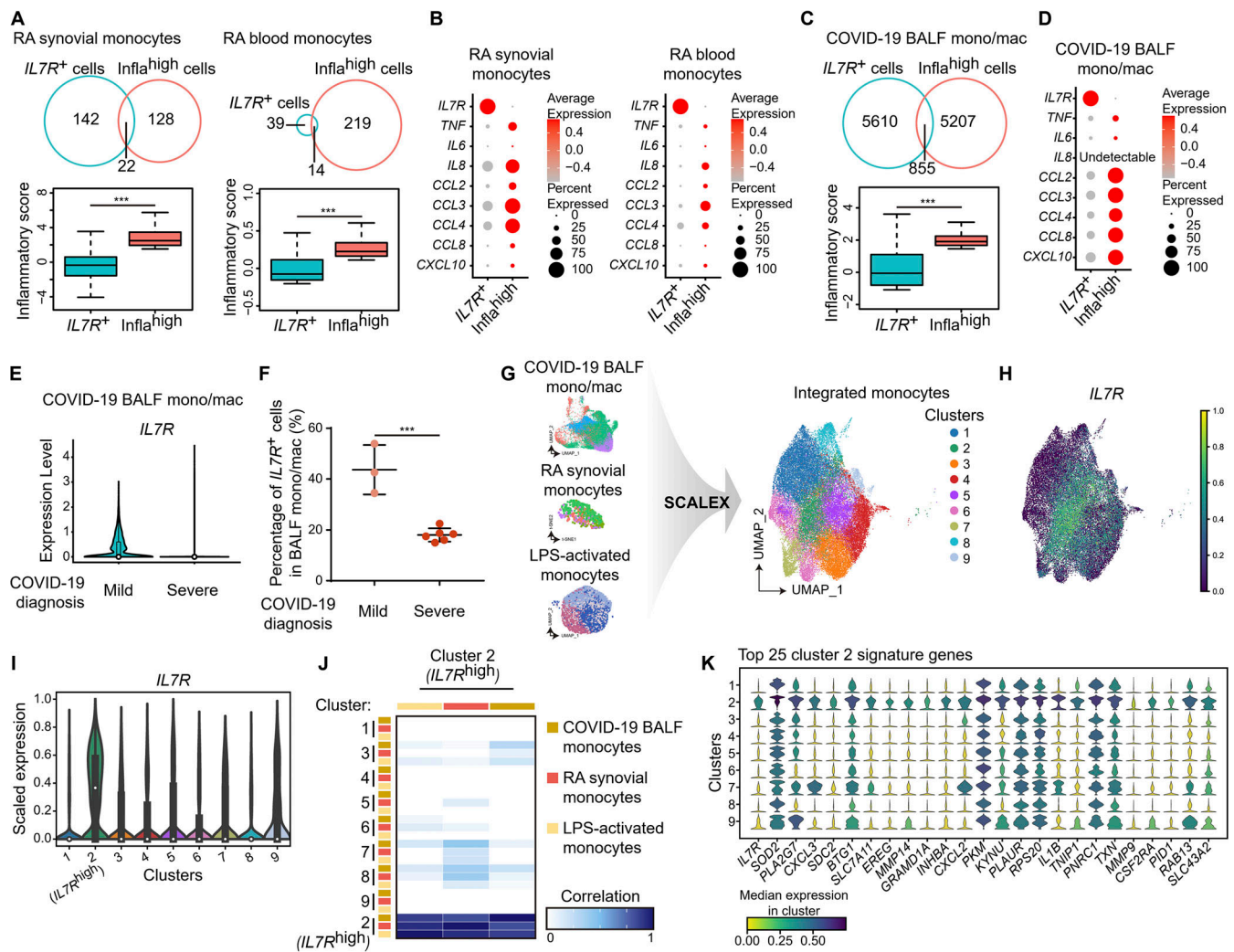
Figure 6. Integrated human inflammatory monocyte expression atlas. (A and C) In monocytes/macrophages (mono/mac) from RA synovia (A, left), RA peripheral blood (A, right), and COVID-19 BALF (C), $IL7R^+$ cells and infla^{high} cells (top 20% inflammatory cells by inflammatory score) were grouped as described in Materials and methods. Venn diagrams (upper) show the extent of overlap between $IL7R^+$ cells and infla^{high} cells with labeling of the cell counts and box plots (bottom) showing the inflammatory score distribution in $IL7R^+$ cells and infla^{high} cells in each disease condition as indicated (see Materials and methods for details in comparison). ***, $P < 0.001$ by Wilcoxon rank-sum test. **(B and D)** Heat maps show the expression of $IL7R$ and eight inflammatory genes for in-flammatory score calculation in $IL7R^+$ cells and infla^{high} cells in mono/mac from each of the disease conditions as indicated. For each gene, scaled average expression level and ratio of expression-positive cells in each cluster are represented by color and size of the dot, respectively. **(E and F)** Mono/mac cells from COVID-19 patient BALF were subdivided by disease severity. Violin plot shows the expression of $IL7R$ in BALF mono/mac from mild or severe COVID-19 patients (E), and each overlaid box indicates the interquartile range with the median shown as a circle. Cumulative dot plot (F) shows percentages of $IL7R^+$ cells in BALF mono/mac from each mild or severe COVID-19 patient as the mean ± SD. ***, $P < 0.001$ by unpaired t test. **(G)** Integration of scRNA-seq datasets for monocytes from COVID-19 BALF, RA synovial tissue, and LPS-activated monocytes was implemented by advanced analysis tool, SCALEX. Nine clusters of in-tegrated monocytes were delimited by unsupervised clustering and are shown in a UMAP plot. **(H)** $IL7R$ expression is expressed by colors and overlaid to a UMAP projection of integrated monocytes in G. **(I)** Violin plot shows the expression of $IL7R$ among nine clusters of integrated monocytes in G. Each overlaid box indicates the interquartile range with the median shown as a circle. Cluster 2 were named the $IL7R^{high}$ cluster (highest $IL7R$ expression). **(J)** For populations of COVID-19 BALF monocytes, RA synovial monocytes, and LPS-treated monocytes, the heat map shows the correlation between cluster 2 cells in each monocyte population and all nine clusters in each monocyte population, respectively. **(K)** The stacked violin plot shows the expression of the top 25 cluster 2 signature genes in all nine monocyte clusters in G. Median expression levels for each gene in each cluster are indicated by colors.

differences in expression levels, because lymphocytic $IL7R$ did not significantly differ between mild and severe patients (Fig. S5 D). These results indicated that CD127 marked a population of hypoinflammatory monocytes/macrophages in vivo and suggested that the prevalence of $IL7R^+$ monocytes/macro-phages likely correlated with subdued inflammation and fa-vorable disease outcomes.

Inspired by the similarity of $IL7R^+$ cells from different disease conditions, we set forth to extrapolate common features of hu-man inflammatory monocytes/macrophages. Aided by a re-cently developed in-house deep learning–driven bioinformatics tool specializing in incorporating single-cell sequencing datasets from multiple sources (Xiong et al., 2021 Preprint), we ran in-tegrated analyses of three datasets: COVID-19 BALF monocytes/

macrophages, RA synovial monocytes, and in vitro LPS-activated monocytes. Unsupervised clustering identified 10 cellular subsets (Fig. S5 E), with cluster 10 classified as *FABP4*-expressing alveolar macrophages from the COVID-19 samples (Fig. S5, F–H) and thus being excluded from the subsequent analyses (Morse et al., 2019). The remaining nine clusters (clusters 1–9) represented integrated monocyte subsets presenting in all three tissue sources (Fig. 6 G and Fig. S5 F), with cluster 2 prominently featured by high *IL7R* expression (Fig. 6, H and I) and sharing a high degree of similarity among three conditions (Fig. 6 J). Common signature genes of cluster 2 revealed a profile that was distinct from the currently known monocyte/macrophage subsets, with *IL7R* unambiguously identified as the top marker gene (Fig. 6 K). Of note, cluster 2 phenotypically differed from the M2-like cells defined by markers such as CD163 (Fig. S5 I). The above advanced informative analyses revealed unifying features of human inflammatory monocytes, regardless of tissue of origin and disease type.

Discussion

During the attempts to investigate in situ phenotypes of human monocytes in COVID-19 and RA patients, single-cell transcriptome analyses revealed a subset of inflammatory monocytes positive for CD127, rendering them sensitive to picogram concentrations of IL-7, a (patho)physiological range detectable in human tissue environments, including blood circulation and lung (Ronit et al., 2021; Venet et al., 2012). Thus, in contrast to the IL-7–inert resting monocytes, upon induction of a receptor subunit, a subset of human monocytes gained IL-7 responsiveness under inflammatory conditions, in line with a previous study reporting active IL-7 signaling measured by JAK3 phosphorylation (Musso et al., 1995). Facilitated by modest up-regulation of the IL-7 cytokine in inflammatory disease settings such as COVID-19 (Ronit et al., 2021), CD127high monocytes actively received environmental IL-7 cues to promote an epigenetically coupled, STAT5-coordinated transcriptional program. Amid the overall inflammatory tissue environments, the CD127–STAT5 axis delivers anti-inflammatory signals, possibly as an attempt to counteract inflammatory signals, to impose functional heterogeneity among human monocytes.

Despite use of various experimental or informatics approaches, we failed to detect CD127 expression in mouse homeostatic and inflammatory monocytes or macrophages, excluding the feasibility of using mice as model organisms for functional and mechanistic investigations. In fact, it has been reported that mouse fetal monocytes express CD127 that is drastically down-regulated in the postnatal stage (Leung et al., 2019). Hence, CD127 expression is silenced in adult mouse monocytes or macrophages, possibly through suppressive epigenetic mechanisms that are irreversible by inflammatory stimuli (Natoli, 2010; Winter and Amit, 2014). Taken together, these results revealed the species-specific nature of monocytic CD127 expression and function.

STAT5 is well recognized to mediate signaling by common γ-chain family cytokines in lymphoid lineages, especially in T cells and ILCs (Leonard et al., 2019). In myeloid lineage cells,

STAT5 activation has been conventionally studied in the context of GM-CSF signaling and has been implicated in cell differentiation and survival (van de Laar et al., 2012; Zhan et al., 2019). However, the role of STAT5 in terminally differentiated myeloid cells such as inflammatory monocytes at the sites of infection remains unclear. Our results implied that STAT5-mediated IL-7 signaling imprints hypoinflammatory phenotypes in CD127high monocytes and thus conveys functional diversity to mature monocyte populations. STAT5 preferentially occupies CD127high feature OCRs, and a majority of STAT5 binding sites displayed enhancer-like characteristics. Interestingly, STAT5-bound putative enhancers were already permissive in resting monocytes before activation, suggesting plausibly heterogeneous epigenetic landscapes among the seemly homogeneous cell population (Carter and Zhao, 2021). Due to the difficulty of performing fate-mapping studies in the human system, comprehensive understanding of the exact lineage and origin of such predefined STAT5-prone monocytes awaits future investigations aided by new technical tools.

Our understanding of human immune cell heterogeneity has been revolutionized by the recent advances in scRNA-seq (Dress et al., 2020; Papalexi and Satija, 2018). Yet, due to difficulties in distinguishing the biologically meaningful differences from technical and/or experimental variations, it remains challenging to compare and contrast single-cell sequencing datasets from multiple sources, especially in human studies where samples have been obtained from different organs under different disease conditions that bear significant intrinsic variabilities. Here, aided by advanced deep learning–based computing tools, we successfully integrated multiple datasets that we and others generated and constructed the expression atlas of human inflammatory monocytes. Intriguingly, inflammatory monocytes derived from multiple disease conditions and multiple tissues showed remarkable similarity in terms of subset stratification and expression profiles, likely implying unifying mechanisms for monocyte activation in vivo. Importantly, the integrated human monocyte phenotypes could not be predicted based on the existing knowledge or extrapolated from model organism–based studies, signifying the necessity of understanding human diseases with human samples. It would be interesting and desirable to assess whether the phenotypes could be observed in additional human disease settings. Given the unique presence of this population in human inflammatory diseases, especially the correlation of expansion of CD127high monocytes with favorable disease outcomes in COVID-19, it is highly conceivable to propose CD127high monocytes and the related CD127/STAT5 pathway as potential therapeutic targets for inflammatory disorders.

Materials and methods

Cell culture and reagents

PBMCs of anonymous healthy donors were isolated from buffy coats purchased from the Beijing Red Cross Blood Center using density gradient cell separation by Ficoll (Lymphoprep; STEMCELL Technologies) following the protocol approved by the institutional review board of the School of Medicine, Tsinghua University. The private information of anonymous blood donors

was inaccessible to investigators. PBMCs of RA patients were obtained from Peking Union Medical College Hospital using the protocol that was approved by the institutional review board of Peking Union Medical College Hospital. CD14$^+$ monocytes were further isolated from PBMCs using anti-CD14 magnetic beads (130-050-201; Miltenyi Biotec). CD14$^+$ monocytes were cultured in RPMI 1640 medium (10040CM; Corning) supplemented with 10% (vol/vol) FBS (Gibco) and human recombinant M-CSF (300-25, 10 ng/ml; PeproTech). LPS (*Escherichia coli* O127:B8; Sigma-Aldrich), human recombinant IL-7 (200-07; PeproTech), human recombinant TNF (H8916; Sigma-Aldrich), or chemical inhibitors (SB203580 from Selleck; STAT5 inhibitor from Santa Cruz Biotechnology; and Bay 11-7082 from Sigma-Aldrich) were used as indicated for various experiments.

Collection of lung tissues and immunohistochemistry

Two cases of uninfected lung tissues and three cases of COVID-19 lung tissues were from the biobank of Southwest Hospital, Third Military Medical University (Army Medical University). COVID-19 lung tissues were obtained during autopsy of the patients who died of SARS-CoV-2 infection. Pathologically normal lung tissues from pulmonary bulla patients were used as uninfected controls. Tissue collection and the following histological analyses were approved by the ethics committee of Southwest Hospital, Third Military Medical University (Army Medical University), and were carried out in accordance with regulations issued by the National Health Commission of China and the Helsinki declaration. Lung tissue sections were stained with hematoxylin for assessment of pulmonary architecture, and anti-CD68 (ab201340; Abcam) and anti-CD127 (PA5-97870; Invitrogen) antibodies were used for immunohistochemistry. Specifically, lung sections were deparaffinized and rehydrated. Antigen retrieval was performed with the Improved Citrate Antigen Retrieval Solution (Beyotime) and incubated with H_2O_2 in the dark for 15 min to block endogenous peroxidase activity. Slides were blocked with 10% goat serum in Tris-buffered saline for 30 min at room temperature and stained with primary antibodies overnight at 4°C. Slides were washed three times with 0.1% Tris-buffered saline with Tween before incubation with HRP-conjugated secondary antibodies (goat anti-rabbit IgG [H&L]–HRP conjugated, BE0101; Bioeasy [Beijing] Technology Co.; goat anti-mouse IgG [H&L]–HRP conjugated, BE0102, Bioeasy [Beijing] Technology Co.). Stained slides were washed again in PBS and stained with diaminobenzidine (Tiangen) in conjunction with a hematoxylin counterstain (Solarbio Life Science). After dehydration, sections were mounted in neutral balsam.

Immunofluorescence histology

COVID-19 lung tissues were collected as described above and were washed and fixed overnight at 4°C in a solution of 1% paraformaldehyde in PBS. The tissues were incubated in a solution of 30% sucrose in PBS and a mixture of 30% sucrose and OCT compound 4583 (Sakura Finetek) separately at 4°C overnight. The samples were then embedded in optimal cutting temperature compound, frozen in a bath of ethanol cooled with liquid nitrogen, and stocked at −80°C. Frozen samples were cut at 10-μm thickness and collected onto slides. Slides were dried at

50°C for 30 min and fixed in 1% paraformaldehyde for 10 min and processed for staining. The tissues were permeabilized in PBS/0.3% Triton X-100/0.3 M glycine at 37°C for 30 min and blocked in PBS/5% goat serum at room temperature for 1 h. The tissues were then incubated with the indicated primary antibodies diluted (anti-CD68, 1:100; anti-CD127, 1:500) in PBS/5% goat serum at 4°C overnight and washed in PBS/0.2% Tween-20 at room temperature for 30 min three times. The tissues were incubated with Alexa Fluor dye–conjugated secondary antibodies (Alexa Fluor 488 goat anti-mouse IgG, 1:500, B40941, Life Technologies; Alexa Fluor 555 goat anti-rabbit IgG, 1:500, A27039, Invitrogen) and DAPI (1:200, C0060-1; Solarbio Life Science) in PBS/0.5% BSA at room temperature for 2 h and washed in PBS/0.2% Tween-20 at room temperature for 1 h five times before mounting with SlowFade Diamond Antifade Mountant (S36963; Life Technologies).

BALF collection for scRNA-seq

Nine COVID-19 patients were enrolled from the Shenzhen Third People's Hospital. BALF collection from COVID-19 patients and healthy donors and the following studies were conducted according to the principles expressed in the Declaration of Helsinki. Ethical approval was obtained from the research ethics committee of Shenzhen Third People's Hospital (2020-112). Diagnosis of COVID-19 was based on clinical symptoms, exposure history, chest radiography, and SARS-CoV-2 RNA positivity. Disease severity was defined as moderate, severe, or critical according to the Diagnosis and Treatment Protocol of COVID-19 issued by the National Health Commission of China. Approximately 20 ml of BALF was obtained from each patient. BALF was directly processed within 2 h, and all operations were performed in a biosafety level 3 laboratory. BALF cells were collected, counted, resuspended, and subsequently processed for scRNA-seq library construction as described in our previous study (Liao et al., 2020). According to the clinical diagnosis, nine enrolled patients included three moderate cases, one severe case, and five critical cases. For the subsequent analyses of scRNA-seq data, given that there was only one clinically defined severe case, the patients were stratified into mild (n = 3) and severe (n = 6, including both severe and critical cases) groups.

Mice

The laboratory animal facility at Tsinghua University has been accredited by the Association for Assessment and Accreditation of Laboratory Animal Care International, and the institutional animal care and use committee of Tsinghua University approved the protocol used in this study for blood collection from mouse cheeks. C57BL/6J mice were bred and housed in isolated ventilated cages (maximum of six mice per cage) at the specific pathogen–free facility at Tsinghua University. The mice were maintained on a 12-h/12-h light/dark cycle in a 22–26°C, 40–70% humidity atmosphere with access to sterile pellet food and water ad libitum.

RNA extraction and quantitative PCR (qPCR)

Total RNA was extracted from cells using TRIzol reagent according to the manufacturer's procedure, and total RNA was

reverse transcribed to cDNA with Moloney murine leukemia virus reverse transcription (2641B; Takara Bio). Real-time qPCR was performed in duplicates with SYBR Green Master Mix (A25742; Applied Biosystems) on a StepOnePlus thermal cycler (Applied Biosystems). Primer sequences are listed for the following genes: *IL7R* (forward) 5′-TCCAACCGGCAGCAATGTAT-3′, (reverse) 5′-TGACCAACAGAGCGACAGAG-3′; *IL2RG* (forward) 5′-GTGCAGCCACTATCTATTCTCTG-3′, (reverse) 5′-GTGAAGTGTTAGGTTCTCTGGAG-3′; *IL6* (forward) 5′-ACCCCCAATAAATATAGGACTGGA-3′, (reverse) 5′-TTCTCTTTCGTTCCCGGTGG-3′; *TNF* (forward) 5′-CCTCTCTCTAATCAGCCCTCTG-3′, (reverse) 5′-GAGGACCTGGGAGTAGATGAG-3′; *MAF* (forward) 5′-ACTGGCAATGAGCAACTCCG-3′, (reverse) 5′-CACTGGCTGATGATGCGGTC-3′.

Flow cytometry
Upon the indicated treatment, cells were collected and washed with staining buffer (PBS with 0.5% BSA and 2 mM EDTA). Then, the surface markers were stained with the indicated fluorochrome-conjugated antibodies in 1:400 dilution for 30 min on ice in the dark. After staining, cells were washed three times with staining buffer and resuspended in PBS for analysis in a BD FACSFortessa sorter or for FACS in a BD FACSAria III sorter. Further data analysis was implemented using FlowJo software (BD Biosciences). For intracellular staining, cells were treated with GolgiStop (554724; BD Biosciences) for 4–5 h before collection. The routine staining for surface markers was performed, after which the cells were fixed with 100 μl/tube fixation buffer (420801; BioLegend) for 25 min at room temperature, and the fixed cells were permeabilized and stained in 1× permeabilization wash buffer with fluorochrome-conjugated antibodies for 30 min on ice in the dark. The fixed and intracellularly stained cells were washed twice with 1× permeabilization wash buffer and suspended in PBS for analysis. The fluorochrome-conjugated antibodies for targets of interest and fluorochrome-conjugated isotype control antibodies were as follows: anti-mouse CD3ε antibody PE (100307; BioLegend), anti-mouse CD11b PerCP-Cyanine5.5 (45-0112-82; eBioscience), anti-mouse CD127 PE-Cyanine7 (135013; BioLegend), anti-mouse MHC class II BV421 (48-5321-82; eBioscience), anti-human CD127 antibody PE-Cyanine5 (351323; BioLegend), anti-human CD14 antibody APC-Cyanine7 (301820; BioLegend), anti-human CD3 antibody FITC (317305; BioLegend), anti-human IL-6 antibody PE (501106; BioLegend), anti-human TNF-α antibody PE (502908; BioLegend), anti-human CD16 antibody BV605 (302039; BioLegend), PE-Cyanine7 rat IgG2a, κ isotype control antibody (400521; BioLegend), and PE rat IgG2b, κ isotype control antibody (400607; BioLegend).

Immunoblotting
Whole-cell lysates were prepared by direct lysis in SDS loading buffer. All samples for immunoblotting were denatured at 95°C for 10 min. For immunoblot analysis, denatured cell lysates were separated by 10% SDS-PAGE and transferred to a polyvinylidene fluoride membrane (EMD Millipore) for probing with specific primary antibodies and HRP-conjugated secondary antibodies. SuperSignal West Pico Chemiluminescent Substrate (34580; Thermo Fisher Scientific) was used for detection. Relative density of blotting bands was quantified using ImageJ (version 1.52a). Antibodies for probing proteins of interest were as follows: anti-GAPDH mouse mAb (BE0023; Bioeasy [Beijing] Technology Co.), anti–β-actin mouse mAb (AC026; Abclonal), anti-phospho-Stat5 (Tyr694) rabbit mAb (9314S; Cell Signaling Technology), anti-Stat5 antibody (9363S; Cell Signaling Technology), anti–c-Maf antibody (sc-518062; Santa Cruz Biotechnology), goat anti-rabbit IgG (H&L)–HRP conjugated (BE0101; Bioeasy [Beijing] Technology Co.), goat anti-mouse IgG (H&L)–HRP conjugated (BE0102; Bioeasy [Beijing] Technology Co.).

ELISA
The concentrations of IL-7 in culture media were measured by ELISA. The culture media were collected after centrifugation for cell pelleting, and the levels of IL-7 were quantified by using the Human IL-7 Quantikine HS ELISA Kit (HS750; R&D Systems) according to the manufacturer's instructions.

Phagocytosis assay
LS 174T human colon epithelial cells were labeled by CellTrace Violet and were subsequently administered with 200 μM H_2O_2 for 8 h to induce apoptosis. Human monocytes were stimulated with LPS for 6 h before coculturing with apoptotic cells for 1 h. Afterward, cell mixtures were stained with anti-human CD127 antibody (PE-Cyanine5) and anti-human CD14 antibody (APC-Cyanine7), and FACS analyses were performed to identify the CD14+ human monocytes with phagocytosed apoptotic cells.

Measurements of NO production
First, CD127^{high} and CD127^{low} monocytes were sorted by FACS from human monocytes upon 6-h LPS stimulation. Approximately 10^6 sorted cells were lysed in 100 μl commercialized Cell and Tissue Lysis Buffer for Nitric Oxide Assay (S3090; Beyotime). Cell lysates were subjected to measurements of NO production by using the Total Nitric Oxide Assay Kit (S0023; Beyotime) according to the manufacturer's instructions. NO measurements were implemented by nitrate reductase–mediated reduction of nitrate and following colorimetric assay with Griess reagent.

RNA interference
Immediately after isolation, primary human monocytes were nucleofected with On-Target Plus SMARTpool siRNA purchased from Dharmacon Inc. specific for *IL7R*, *MAF*, or *MAP3K3*. Nontargeting siRNA from GenePharma was used as a control. Human Monocyte Nucleofector buffer (V4XP-3024; Lonza) and the Lonza 4D-Nucleofector platform were used according to the manufacturer's instructions with the human monocyte nucleofection program. The nucleofected monocytes were cultured in RPMI 1640 medium (Corning) supplemented with 10% (vol/vol) FBS (Gibco) and human recombinant M-CSF (20 ng/ml; PeproTech) for 48 h before the following experiments.

ChIP assay
For STAT5 ChIP-seq assays, CD14+ selected human monocytes were stimulated with LPS (10 ng/ml) for 6 h. Approximately $30 × 10^6$ stimulated cells were first stained for surface CD127 and

then fixed in 1% methanol-free formaldehyde (Thermo Fisher Scientific) for 8 min at room temperature followed by quenching with 125 mM glycine for another 5 min. FACS-based cell sorting implemented the isolation of CD127^{high} monocytes from fixed cells. Approximately 15 × 10^{6} CD127^{high} monocytes were used for ChIP. The ChIP assay was performed using the SimpleChIP enzymatic ChIP kit (Cell Signaling Technology) according to the manufacturer's instructions. The DNA–protein complexes were immunoprecipitated using 10 µl per sample of STAT5 antibody (9363S; Cell Signaling Technology). The immunoprecipitated DNA fragments were extracted with the QIAquick PCR purification kit (Qiagen) and subjected to ChIP-seq library construction with NEBNext Ultra II DNA Library Prep kit (E7103S; New England Biolabs). The constructed DNA library was sent for sequencing on an Illumina HiSeq X Ten platform for an average of 20 million unique reads per sample.

For STAT5 ChIP-qPCR assays, THP-1 cells were stimulated with LPS (100 ng/ml) for 6 h and subsequently with IL-7 (10 ng/ml) for 30 min. 10–20 × 10^{6} cells per condition were used for ChIP experiments as described above by using STAT5 antibody (9363S; Cell Signaling Technology) and IgG (2729P; Cell Signaling Technology) control. The immunoprecipitated DNA fragments were extracted with the QIAquick PCR purification kit (Qiagen) and subjected to qPCR assay for enrichment detection in the *MAF* TSS upstream GAS motif with the following primer pair: (forward) 5′-AAGTGCAGTGCTATAAAGTTGTTT-3′ and (reverse) 5′-ATGTTCAAGACGCTGGCTTA-3′.

RNA-seq
Human CD14^{+} monocytes were stimulated with LPS 10 ng/ml for 6 h, and CD127^{high} and CD127^{low} populations for each donor were sorted by FACS. Total RNA was extracted from CD127^{high} and CD127^{low} cells using TRIzol reagent (Thermo Fisher Scientific) according to the manufacturer's procedure, and RNA samples were processed for library construction with the TruSeq mRNA-seq Sample Preparation Kit (Illumina) and sequencing by BGI Genomics Co. on a BGISEQ-500RS platform. Three independent sets of paired samples collected from three healthy donors were subjected to RNA-seq and the subsequent bioinformatics analyses.

scRNA-seq for RA PBMCs and LPS-activated monocytes
After the isolation or treatment, cells were frozen in FBS + 10% DMSO for preservation in liquid nitrogen. The frozen cells were processed for scRNA-seq by BGI Genomics Co. Single-cell capturing and downstream library construction were performed using Chromium Single Cell 3′ Reagent kits (10x Genomics) according to the manufacturer's protocol. The constructed libraries were sequenced on a BGI MGISEQ2000 platform.

ATAC-seq
Human CD14^{+} monocytes from healthy donors were stimulated with 10 ng/ml of LPS for 6 h, and CD127^{high} and CD127^{low} populations for each donor were sorted by FACS. Cells were pelleted by centrifugation for 10 min at 500 *g* and 4°C using a swing rotor with low acceleration and brake settings. Cell pellets were washed once with 1× PBS, and cells were pelleted again by

centrifugation using the previous settings. Cell pellets were resuspended in 50 µl of lysis buffer (10 mM Tris-HCl, pH 7.4, 10 mM NaCl, 3.0 mM MgCl₂, and 0.5% NP-40), and nuclei were pelleted by centrifugation for 30 min at 500 *g* and 4°C using a swing rotor with low acceleration and brake settings. The supernatant was discarded, and nuclei were resuspended in 50 µl reaction buffer containing 5.0 µl Tn5 transposase and 10 µl 5× TruPrep Tagment Buffer L (TruePrep DNA Library Prep Kit V2 for Illumina; Vazyme Biotech). The reaction was incubated at 37°C for 30 min. After the tagmentation, the transposed DNA fragments were purified by 1× AMPure XP beads (Beckman Coulter). PCR was performed to amplify the libraries for nine cycles using the following PCR conditions: 72°C for 3 min; 98°C for 30 s; and thermocycling at 98°C for 15 s, 60°C for 30 s, and 72°C for 3 min; followed by 72°C for 5 min. After the PCR, libraries were purified with the 0.5× and 1.2× AMPure XP beads. DNA concentrations were measured with the StepOnePlus Real-Time PCR System (Life Technologies), and library sizes were determined using an Agilent 2100 Bioanalyzer. Libraries were sequenced on an Illumina HiSeq X Ten platform for an average of 20 million unique reads per sample. Three independent sets of paired samples collected from three healthy donors were subjected to ATAC-seq and the subsequent bioinformatics analyses.

Next-generation sequencing data alignment
ATAC-seq paired-end reads were collected. Adapter sequences were trimmed from the ends of reads by Cutadapt (version 1.14), and the reads that failed to pass the quality control (Q > 10) were discarded. STAT5 ChIP-seq paired-end reads were collected at 150 bp in length. The first-end reads were used for analyses and trimmed to 50 bp, and adapter sequences were further trimmed from the ends of reads by Cutadapt (version 1.14). The reads that failed to pass the quality control (Q > 10) were discarded. H3K27ac and H3K4me1 ChIP-seq datasets were downloaded from the National Center for Biotechnology Information Gene Expression Omnibus (GEO) dataset under the GEO accession no. GSE85245 (Novakovic et al., 2016), and MAF ChIP-seq datasets were obtained from GEO accession no. GSE98369 (Kang et al., 2017). The ATAC-seq datasets for resting and LPS 4 h stimulated human monocytes were downloaded from GEO accession no. GSE98369 (Kang et al., 2017) and GEO accession no. GSE120942 (Kang et al., 2019), respectively. Sequence Read Archive files were converted to fastq files using fastq-dump included in the Sequence Read Archive toolkit. Both single-end and paired-end ATAC-seq reads were aligned to the human genome (University of California, Santa Cruz hg38) using Bowtie2 (version 2.2.5; Langmead and Salzberg, 2012) with no more than one mismatch for each alignment seed with 15 bp in length to generate alignment files of uniquely mapped single-end reads or uniquely mapped paired-end fragments with maximum length of 1,000 bp. ChIP-seq reads in fastq files were aligned to the human genome (University of California, Santa Cruz hg38) using Bowtie (version 1.1.2; Langmead et al., 2009) to generate alignment files of uniquely mapped reads with maximum allowed mismatch of 2 (-m 1 -n 2) for each alignment seed. ChIP-seq reads aligned to the genome were extended to 150 bp from their 3′ end for

further analyses. RNA-seq data were collected, and single-end reads were aligned to the human genome (hg38) using TopHat (version 2.1.0; Kim et al., 2013) with the parameters --min-segment-intron 50 --no-novel-indels --no-coverage-search, and only uniquely mapped reads were preserved.

Identification of OCRs by ATAC-seq and visualization of ATAC-seq and ChIP-seq datasets

The ATAC-seq alignment files for CD127^{high} and CD127^{low} monocytes from three donors were used to call peaks for significantly opened chromatin regions using MACS2 (version 2.1.1; false discovery rate <0.05). The peaks from six samples were merged as total OCRs in LPS-treated monocytes. To identify the differentially opened chromatin regions between CD127^{high} and CD127^{low} monocytes, the ATAC-seq fragments were counted in each OCR for each sample by using FeatureCounts (version 1.5.0; Liao et al., 2014). Subsequently, the fragment count was normalized to count per million mapped fragments for each sample. The normalized fragment count was used to identify differentially opened chromatin regions by edgeR (version 3.28.1; Robinson et al., 2010). Mean values of (fragment count + 1) fold change (CD127^{high}/CD127^{low}) among three donors were log$_2$ transformed, and differentially opened chromatin regions were identified by log$_2$-transformed fold changes (CD127^{high}/CD127^{low}) ≥1 or less than or equal to –1 for CD127^{high} monocyte feature OCRs or CD127^{low} monocyte feature OCRs with cutoff of P < 0.05. The STAT5 ChIP-seq alignment file was used to call peaks for significantly STAT5-enriched regions using MACS2 (version 2.1.1; false discovery rate <0.05). To visualize ATAC-seq and ChIP-seq signals around genome regions of interest, we first counted ATAC-seq fragments (-fragLength given) and ChIP-seq extended reads (-fragLength 150) every 10 bp from the center of OCRs or STAT5 peaks to ±2.5-kb regions for each OCR or STAT5 peak by using the annotatePeaks.pl program in HOMER (version 4.7.2; Heinz et al., 2010). The output counting matrices were visualized by using Cluster TreeView (version 1.2.0) and were further used to generate average signals around OCRs by calculating the average fragments/reads count per bin (10 bp) per OCR.

RNA-seq data analyses

For coverage of mapped RNA-seq reads in transcripts, the expression level of each gene transcript was calculated as the normalized read count per kilobase of transcript per million mapped reads (fragments per kilobase per million mapped reads [FPKM]) using Cufflinks (version 2.2.1; Trapnell et al., 2012). Differential gene expression between CD127^{high} and CD127^{low} monocytes from three donors was identified using DESeq2 (version 1.27.9; Love et al., 2014). Genes with P < 0.05 and mean (FPKM + 1) fold changes (CD127^{high}/CD127^{low}) ≥1.5 or ≤0.67 among three donors were defined as highly expressed genes in CD127^{high} monocytes or highly expressed genes in CD127^{low} monocytes, respectively. The expression data (gene-specific transcripts per million total transcripts) of published RNA-seq datasets for macrophages and monocytes isolated from mouse lung tissues under LPS-induced pulmonary inflammation were downloaded from the GEO DataSets under accession no. GSE136914 (Sajti et al., 2020).

scRNA-seq data analyses

For scRNA-seq of COVID-19 patients' BALF cells, the Cell Ranger software suite (version 3.1.0) was used to perform sample demultiplexing, barcode processing, and single-cell 5′ unique molecular identifier (UMI) counting. Specifically, splicing-aware aligner STAR was used in FASTQs alignment. Cell barcodes were then determined based on the distribution of UMI counts automatically, and the gene–barcode matrices were saved for downstream analyses. In addition, one additional healthy control was acquired from the GEO database under accession no. GSE128033. All samples were loaded as Seurat objects by using Seurat (version 3.2.1; Stuart et al., 2019), and quality control for each cell was conducted with the following criteria: gene number between 200 and 6,000, UMI count >1,000, and mitochondrial gene percentage <0.1. All samples were further integrated to remove the batch effects with the parameter settings of the first 50 dimensions of canonical correlation analysis and principal component analysis (PCA). The integrated Seurat project was first normalized, and the top 2,000 variable genes were then identified by using the Seurat analysis pipeline that has been described in our previous studies. Gene expression scaling and PCA were performed using the top 2,000 variable genes. Then, Uniform Manifold Approximation and Projection (UMAP) was performed on the top 50 principal components for visualization, and graph-based clustering was simultaneously performed on the PCA-reduced data with the 1.2 resolution setting. According to the clustering result, 32 clusters were identified, and the annotations for each cluster were implemented based on the expression of marker genes that were used in our previous study (Liao et al., 2020). Monocytes/macrophages (CD14^{high} CD68^{high}) were extracted from the total BALF cells after annotation, and reclustering (PCA and UMAP) was performed. The clusters showing expression of both monocyte/macrophage marker genes and T cell marker genes were excluded as doublets. Only the cells from COVID-19 patients were used for downstream analyses of both total BALF cells and monocytes/macrophages.

RA synovial scRNA-seq datasets (Zhang et al., 2019a) were downloaded from ImmPort with the study accession code of SDY998. The reduction and clustering results from the original study were used. The monocyte clusters were extracted for downstream analyses.

The Cell Ranger software suite (version 3.1.0) was used to perform sample demultiplexing, barcode processing, and single-cell 5′ UMI counting, and gene–barcode matrices were generated for LPS-treated human CD14$^+$ monocytes and RA patient PBMCs. The gene–barcode matrices were loaded as Seurat objects, and quality control for each cell was performed with criteria for LPS-treated human CD14$^+$ monocytes (gene number between 200 and 4,500, UMI count >1,000, and mitochondrial gene percentage <0.15) and RA PBMCs (gene number between 200 and 6,000, UMI count >1,000, and mitochondrial gene percentage <0.1). After quality control, the top 2,000 variable genes were identified, and gene expression scaling, PCA, and UMAP clustering were performed for each dataset. Marker genes for each cluster in each scRNA-seq dataset were identified by using the FindAllMarkers function in Seurat. According to the expression of well-studied PBMC marker genes summarized in the

Zhang et al.
CD127 imprints hypoinflammatory human monocytes

Journal of Experimental Medicine   14 of 17
https://doi.org/10.1084/jem.20211191

CellMarker website (Zhang et al., 2019b), each cluster of RA PBMCs was annotated with a certain cell type, and monocyte clusters were extracted for downstream analyses.

IL7R⁺ cells were identified based on the normalized expression (>0) of *IL7R* for each cell in each scRNA-seq dataset. Inflammatory score was calculated based on the normalized average expression of eight inflammatory genes: *TNF*, *IL6*, *IL8*, *CCL2*, *CCL3*, *CCL4*, *CCL8*, and *CXCL10*, which is implemented by the AddModuleScore function in Seurat with 100 controls for each inflammatory gene. The inflammatory genes were chosen based on their induction by LPS stimulation and inflammatory properties that have been widely used to profile the characteristics of macrophages or monocytes in diseases, especially RA and COVID-19 (Kuo et al., 2019; Liao et al., 2020). We also precluded the inflammatory genes whose products are subjected to extensive post-transcriptional regulation, such as *IL1B*. Inflammatory monocytes (infla^{high}) in each set of scRNA-seq data were identified as the top 20% inflammatory cells based on inflammatory score in monocytes/macrophages from RA synovia, RA peripheral blood, and COVID-19 BALF, respectively. *IL7R* positivity was prioritized over infla^{high} to enable the comparison between two distinct *IL7R*⁺ and infla^{high} populations in each condition.

Integration of COVID-19 monocytes/macrophages, RA synovial monocytes, and LPS-treated monocytes was implemented by a recently developed SCALEX method based on the asymmetric variational autoencoder framework as shown in Fig. S5 E (Xiong et al., 2021). In brief, the training of SCALEX was to maximize the likelihood of imputed scRNA-seq data to their original ones without batch effect, which could be transformed to maximize the evidence lower bound and expressed with a reconstruction term and a regularization term as shown in Fig. S5 E. The reconstruction term coaches the imputation of data to be similar to their inputs, and the regularization term is a Kullback-Leibler divergence to regularize the latent variable *z* to a Gaussian mixture model manifold. Leiden clustering and UMAP visualization were performed based on the features extracted by SCALEX for integrated monocytes/macrophages, and marker genes for each cluster were identified. Correlations between clusters among three datasets were calculated as Pearson correlation coefficients, and the negative values were normalized to 0 for heat map presentation.

Statistical analysis

Types of statistical tests are indicated in the figure legends. Statistical analyses were performed using GraphPad Prism software (GraphPad Software) for *t* test (Student's *t* test), and the Wilcoxon rank-sum test was implemented using R (version 4.0.2). P < 0.05 was considered statistically significant.

Online supplemental material

Fig. S1 shows the results of clustering analyses for scRNA-seq datasets of COVID-19 patients' BALF and RA patients' synovial tissues. Fig. S2 shows the characterizations of elicited CD127 expression in activated human monocytes, including the comparable CD127 positivity in activated monocytes to T cells, dependency on TLR-mediated signaling pathways, commonly up-regulated CD127 expression among CD14-CD16 segmented human monocyte populations, and human-specific nature of such monocytic CD127 expression. Fig. S3 shows the comparable monocyte functions, such as NO production and phagocytosis, between CD127^{high} and CD127^{low} monocytes and the functional anti-inflammatory IL-7 receptor signaling in activated human monocytes. Fig. S4 shows CD127 expression coordinated epigenetic landscapes in CD127^{high} and CD127^{low} monocytes and MAF-regulated anti-inflammatory expression profile in human monocytes. Fig. S5 presents the results of further analyses for scRNA-seq datasets, including clustering analysis for the scRNA-seq dataset of RA patient PBMCs, profiling CD127 expression according to the disease severity in monocytes/macrophages and lymphoid lineage cells from COVID-19 patient BALF, integrative analysis for monocytes/macrophages from multiple inflammatory conditions, and designating specific monocyte/macrophage subsets via the integrative analysis.

Data availability

Sequencing datasets are deposited in the GEO with assigned accession numbers as follows: RNA-seq and ATAC-seq (GEO accession no. GSE159118), STAT5 ChIP-seq (GEO accession no. GSE173490), healthy donor scRNA-seq (GEO accession no. GSE159113), RA scRNA-seq (GEO accession no. GSE159117), and COVID-19 BALF scRNA-seq (GEO accession no. GSE145926).

supervised experiments, analyzed and interpreted data, and wrote the manuscript.

Disclosures: The authors declare no competing interests exist.

References

Al-Mossawi, H., N. Yager, C.A. Taylor, E. Lau, S. Danielli, J. de Wit, J. Gilchrist, I. Nassiri, E.A. Mahe, W. Lee, et al. 2019. Context-specific regulation of surface and soluble IL7R expression by an autoimmune risk allele. *Nat. Commun.* 10:4575. https://doi.org/10.1038/s41467-019-12393-1

Barata, J.T., S.K. Durum, and B. Seddon. 2019. Flip the coin: IL-7 and IL-7R in health and disease. *Nat. Immunol.* 20:1584–1593. https://doi.org/10.1038/s41590-019-0479-x

Carter, B., and K. Zhao. 2021. The epigenetic basis of cellular heterogeneity. *Nat. Rev. Genet.* 22:235–250.

Chen, Z., S.J. Kim, N.D. Chamberlain, S.R. Pickens, M.V. Volin, S. Volkov, S. Arami, J.W. Christman, B.S. Prabhakar, W. Swedler, et al. 2013. The novel role of IL-7 ligation to IL-7 receptor in myeloid cells of rheumatoid arthritis and collagen-induced arthritis. *J. Immunol.* 190:5256–5266. https://doi.org/10.4049/jimmunol.1201675

Cormican, S., and M.D. Griffin. 2020. Human monocyte subset distinctions and function: insights from gene expression analysis. *Front. Immunol.* 11:1070. https://doi.org/10.3389/fimmu.2020.01070

Donlin, L.T., S.H. Park, E. Giannopoulou, A. Ivovic, K.H. Park-Min, R.M. Siegel, and L.B. Ivashkiv. 2019. Insights into rheumatic diseases from next-generation sequencing. *Nat. Rev. Rheumatol.* 15:327–339. https://doi.org/10.1038/s41584-019-0217-7

Dress, R.J., Z. Liu, and F. Ginhoux. 2020. Towards the better understanding of myelopoiesis using single-cell technologies. *Mol. Immunol.* 122:186–192. https://doi.org/10.1016/j.molimm.2020.04.020

Ermann, J., D.A. Rao, N.C. Teslovich, M.B. Brenner, and S. Raychaudhuri. 2015. Immune cell profiling to guide therapeutic decisions in rheumatic diseases. *Nat. Rev. Rheumatol.* 11:541–551. https://doi.org/10.1038/nrrheum.2015.71

Godec, J., Y. Tan, A. Liberzon, P. Tamayo, S. Bhattacharya, A.J. Butte, J.P. Mesirov, and W.N. Haining. 2016. Compendium of immune signatures identifies conserved and species-specific biology in response to inflammation. *Immunity.* 44:194–206. https://doi.org/10.1016/j.immuni.2015.12.006

Guilliams, M., A. Mildner, and S. Yona. 2018. Developmental and functional heterogeneity of monocytes. *Immunity.* 49:595–613. https://doi.org/10.1016/j.immuni.2018.10.005

Hagai, T., X. Chen, R.J. Miragaia, R. Rostom, T. Gomes, N. Kunowska, J. Henriksson, J.E. Park, V. Proserpio, G. Donati, et al. 2018. Gene expression variability across cells and species shapes innate immunity. *Nature.* 563:197–202. https://doi.org/10.1038/s41586-018-0657-2

Heinz, S., C. Benner, N. Spann, E. Bertolino, Y.C. Lin, P. Laslo, J.X. Cheng, C. Murre, H. Singh, and C.K. Glass. 2010. Simple combinations of lineage-determining transcription factors prime cis-regulatory elements required for macrophage and B cell identities. *Mol. Cell.* 38:576–589. https://doi.org/10.1016/j.molcel.2010.05.004

Hu, X., A.Y. Chung, I. Wu, J. Foldi, J. Chen, J.D. Ji, T. Tateya, Y.J. Kang, J. Han, M. Gessler, et al. 2008. Integrated regulation of Toll-like receptor responses by Notch and interferon-γ pathways. *Immunity.* 29:691–703. https://doi.org/10.1016/j.immuni.2008.08.016

Kalliolias, G.D., and L.B. Ivashkiv. 2016. TNF biology, pathogenic mechanisms and emerging therapeutic strategies. *Nat. Rev. Rheumatol.* 12:49–62. https://doi.org/10.1038/nrrheum.2015.169

Kang, K., S.H. Park, J. Chen, Y. Qiao, E. Giannopoulou, K. Berg, A. Hanidu, J. Li, G. Nabozny, K. Kang, et al. 2017. Interferon-γ represses M2 gene expression in human macrophages by disassembling enhancers bound by the transcription factor MAF. *Immunity.* 47:235–250.e4. https://doi.org/10.1016/j.immuni.2017.07.017

Kang, K., M. Bachu, S.H. Park, K. Kang, S. Bae, K.H. Park-Min, and L.B. Ivashkiv. 2019. IFN-γ selectively suppresses a subset of TLR4-activated genes and enhancers to potentiate macrophage activation. *Nat. Commun.* 10:3320. https://doi.org/10.1038/s41467-019-11147-3

Kim, D., G. Pertea, C. Trapnell, H. Pimentel, R. Kelley, and S.L. Salzberg. 2013. TopHat2: accurate alignment of transcriptomes in the presence of insertions, deletions and gene fusions. *Genome Biol.* 14:R36. https://doi.org/10.1186/gb-2013-14-4-r36

Kim, S.J., H.J. Chang, M.V. Volin, S. Umar, K. Van Raemdonck, A. Chevalier, K. Palasiewicz, J.W. Christman, S. Volkov, S. Arami, et al. 2020. Macrophages are the primary effector cells in IL-7-induced arthritis. *Cell. Mol. Immunol.* 17:728–740.

Kuo, D., J. Ding, I.S. Cohn, F. Zhang, K. Wei, D.A. Rao, C. Rozo, U.K. Sokhi, S. Shanaj, D.J. Oliver, et al. 2019. HBEGF+ macrophages in rheumatoid arthritis induce fibroblast invasiveness. *Sci. Transl. Med.* 11:eaau8587. https://doi.org/10.1126/scitranslmed.aau8587

Langmead, B., and S.L. Salzberg. 2012. Fast gapped-read alignment with Bowtie 2. *Nat. Methods.* 9:357–359. https://doi.org/10.1038/nmeth.1923

Langmead, B., C. Trapnell, M. Pop, and S.L. Salzberg. 2009. Ultrafast and memory-efficient alignment of short DNA sequences to the human genome. *Genome Biol.* 10:R25. https://doi.org/10.1186/gb-2009-10-3-r25

Leonard, W.J., J.X. Lin, and J.J. O'Shea. 2019. The γc family of cytokines: basic biology to therapeutic ramifications. *Immunity.* 50:832–850. https://doi.org/10.1016/j.immuni.2019.03.028

Leung, G.A., T. Cool, C.H. Valencia, A. Worthington, A.E. Beaudin, and E.C. Forsberg. 2019. The lymphoid-associated interleukin 7 receptor (IL7R) regulates tissue-resident macrophage development. *Development.* 146:dev176180. https://doi.org/10.1242/dev.176180

Liao, Y., G.K. Smyth, and W. Shi. 2014. featureCounts: an efficient general purpose program for assigning sequence reads to genomic features. *Bioinformatics.* 30:923–930. https://doi.org/10.1093/bioinformatics/btt656

Liao, M., Y. Liu, J. Yuan, J. Wen, G. Xu, J. Zhao, L. Cheng, J. Li, X. Wang, F. Wang, et al. 2020. Single-cell landscape of bronchoalveolar immune cells in patients with COVID-19. *Nat. Med.* 26:842–844. https://doi.org/10.1038/s41591-020-0901-9

Locati, M., G. Curtale, and A. Mantovani. 2020. Diversity, mechanisms, and significance of macrophage plasticity. *Annu. Rev. Pathol.* 15:123–147. https://doi.org/10.1146/annurev-pathmechdis-012418-012718

Love, M.I., W. Huber, and S. Anders. 2014. Moderated estimation of fold change and dispersion for RNA-seq data with DESeq2. *Genome Biol.* 15:550. https://doi.org/10.1186/s13059-014-0550-8

Martinez, F.O., S. Gordon, M. Locati, and A. Mantovani. 2006. Transcriptional profiling of the human monocyte-to-macrophage differentiation and polarization: new molecules and patterns of gene expression. *J. Immunol.* 177:7303–7311. https://doi.org/10.4049/jimmunol.177.10.7303

Merad, M., and J.C. Martin. 2020. Pathological inflammation in patients with COVID-19: a key role for monocytes and macrophages. *Nat. Rev. Immunol.* 20:355–362. https://doi.org/10.1038/s41577-020-0331-4

Morse, C., T. Tabib, J. Sembrat, K.L. Buschur, H.T. Bittar, E. Valenzi, Y. Jiang, D.J. Kass, K. Gibson, W. Chen, et al. 2019. Proliferating SPP1/MERTK-expressing macrophages in idiopathic pulmonary fibrosis. *Eur. Respir. J.* 54:1802441. https://doi.org/10.1183/13993003.02441-2018

Musso, T., J.A. Johnston, D. Linnekin, L. Varesio, T.K. Rowe, J.J. O'Shea, and D.W. McVicar. 1995. Regulation of JAK3 expression in human monocytes: phosphorylation in response to interleukins 2, 4, and 7. *J. Exp. Med.* 181:1425–1431. https://doi.org/10.1084/jem.181.4.1425

Nathan, C., and A. Ding. 2010. Nonresolving inflammation. *Cell.* 140:871–882. https://doi.org/10.1016/j.cell.2010.02.029

Natoli, G. 2010. Maintaining cell identity through global control of genomic organization. *Immunity.* 33:12–24. https://doi.org/10.1016/j.immuni.2010.07.006

Novakovic, B., E. Habibi, S.Y. Wang, R.J.W. Arts, R. Davar, W. Megchelenbrink, B. Kim, T. Kuznetsova, M. Kox, J. Zwaag, et al. 2016. β-Glucan reverses the epigenetic state of LPS-induced immunological tolerance. *Cell.* 167:1354–1368.e14. https://doi.org/10.1016/j.cell.2016.09.034

Papalexi, E., and R. Satija. 2018. Single-cell RNA sequencing to explore immune cell heterogeneity. *Nat. Rev. Immunol.* 18:35–45. https://doi.org/10.1038/nri.2017.76

Pickens, S.R., N.D. Chamberlain, M.V. Volin, R.M. Pope, N.E. Talarico, A.M. Mandelin II, and S. Shahrara. 2011. Characterization of interleukin-7 and interleukin-7 receptor in the pathogenesis of rheumatoid arthritis. *Arthritis Rheum.* 63:2884–2893. https://doi.org/10.1002/art.30493

Robinson, M.D., D.J. McCarthy, and G.K. Smyth. 2010. edgeR: a Bioconductor package for differential expression analysis of digital gene expression data. *Bioinformatics.* 26:139–140. https://doi.org/10.1093/bioinformatics/btp616

Ronit, A., R.M.G. Berg, J.T. Bay, A.K. Haugaard, M.G. Ahlström, K.S. Burgdorf, H. Ullum, S.B. Rørvig, K. Tjelle, N.B. Foss, et al. 2021. Compartmental

immunophenotyping in COVID-19 ARDS: A case series. *J. Allergy Clin. Immunol.* 147:81–91. https://doi.org/10.1016/j.jaci.2020.09.009

Sajti, E., V.M. Link, Z. Ouyang, N.J. Spann, E. Westin, C.E. Romanoski, G.J. Fonseca, L.S. Prince, and C.K. Glass. 2020. Transcriptomic and epigenetic mechanisms underlying myeloid diversity in the lung. *Nat. Immunol.* 21:221–231. https://doi.org/10.1038/s41590-019-0582-z

Schroder, K., K.M. Irvine, M.S. Taylor, N.J. Bokil, K.A. Le Cao, K.A. Masterman, L.I. Labzin, C.A. Semple, R. Kapetanovic, L. Fairbairn, et al. 2012. Conservation and divergence in Toll-like receptor 4-regulated gene expression in primary human versus mouse macrophages. *Proc. Natl. Acad. Sci. USA.* 109:E944–E953. https://doi.org/10.1073/pnas.1110156109

Shay, T., V. Jojic, O. Zuk, K. Rothamel, D. Puyraimond-Zemmour, T. Feng, E. Wakamatsu, C. Benoist, D. Koller, and A. Regev. ImmGen Consortium. 2013. Conservation and divergence in the transcriptional programs of the human and mouse immune systems. *Proc. Natl. Acad. Sci. USA.* 110: 2946–2951. https://doi.org/10.1073/pnas.1222738110

Shi, C., and E.G. Pamer. 2011. Monocyte recruitment during infection and inflammation. *Nat. Rev. Immunol.* 11:762–774. https://doi.org/10.1038/nri3070

Stuart, T., A. Butler, P. Hoffman, C. Hafemeister, E. Papalexi, W.M. Mauck III, Y. Hao, M. Stoeckius, P. Smibert, and R. Satija. 2019. Comprehensive integration of single-cell data. *Cell.* 177:1888–1902.e21.

Trapnell, C., A. Roberts, L. Goff, G. Pertea, D. Kim, D.R. Kelley, H. Pimentel, S.L. Salzberg, J.L. Rinn, and L. Pachter. 2012. Differential gene and transcript expression analysis of RNA-seq experiments with TopHat and Cufflinks. *Nat. Protoc.* 7:562–578. https://doi.org/10.1038/nprot.2012.016

Vabret, N., G.J. Britton, C. Gruber, S. Hegde, J. Kim, M. Kuksin, R. Levantovsky, L. Malle, A. Moreira, M.D. Park, et al. Sinai Immunology Review Project. 2020. Immunology of COVID-19: current state of the science. *Immunity.* 52:910–941. https://doi.org/10.1016/j.immuni.2020.05.002

van de Laar, L., P.J. Coffer, and A.M. Woltman. 2012. Regulation of dendritic cell development by GM-CSF: molecular control and implications for immune homeostasis and therapy. *Blood.* 119:3383–3393. https://doi.org/10.1182/blood-2011-11-370130

van der Poll, T., F.L. van de Veerdonk, B.P. Scicluna, and M.G. Netea. 2017. The immunopathology of sepsis and potential therapeutic targets. *Nat. Rev. Immunol.* 17:407–420. https://doi.org/10.1038/nri.2017.36

Venet, F., A.P. Foray, A. Villars-Méchin, C. Malcus, F. Poitevin-Later, A. Lepape, and G. Monneret. 2012. IL-7 restores lymphocyte functions in septic patients. *J. Immunol.* 189:5073–5081. https://doi.org/10.4049/jimmunol.1202062

Winter, D.R., and I. Amit. 2014. The role of chromatin dynamics in immune cell development. *Immunol. Rev.* 261:9–22. https://doi.org/10.1111/imr.12200

Xiong, L., K. Tian, Y. Li, and Q.C. Zhang. 2021. Online single-cell data integration through projecting heterogeneous datasets into a common cell-embedding space. *bioRxiv.* (Preprint posted October 11, 2021)https://doi.org/10.21203/rs.3.rs-398163/v1

Yoshida, H., C.A. Lareau, R.N. Ramirez, S.A. Rose, B. Maier, A. Wroblewska, F. Desland, A. Chudnovskiy, A. Mortha, C. Dominguez, et al. Immunological Genome Project. 2019. The *cis*-regulatory atlas of the mouse immune system. *Cell.* 176:897–912.e20. https://doi.org/10.1016/j.cell.2018.12.036

Zhan, Y., A.M. Lew, and M. Chopin. 2019. The pleiotropic effects of the GM-CSF rheostat on myeloid cell differentiation and function: more than a numbers game. *Front. Immunol.* 10:2679. https://doi.org/10.3389/fimmu.2019.02679

Zhang, F., K. Wei, K. Slowikowski, C.Y. Fonseka, D.A. Rao, S. Kelly, S.M. Goodman, D. Tabechian, L.B. Hughes, K. Salomon-Escoto, et al. Accelerating Medicines Partnership Rheumatoid Arthritis and Systemic Lupus Erythematosus (AMP RA/SLE) Consortium. 2019a. Defining inflammatory cell states in rheumatoid arthritis joint synovial tissues by integrating single-cell transcriptomics and mass cytometry. *Nat. Immunol.* 20:928–942. https://doi.org/10.1038/s41590-019-0378-1

Zhang, X., Y. Lan, J. Xu, F. Quan, E. Zhao, C. Deng, T. Luo, L. Xu, G. Liao, M. Yan, et al. 2019b. CellMarker: a manually curated resource of cell markers in human and mouse. *Nucleic Acids Res.* 47(D1):D721–D728. https://doi.org/10.1093/nar/gky900
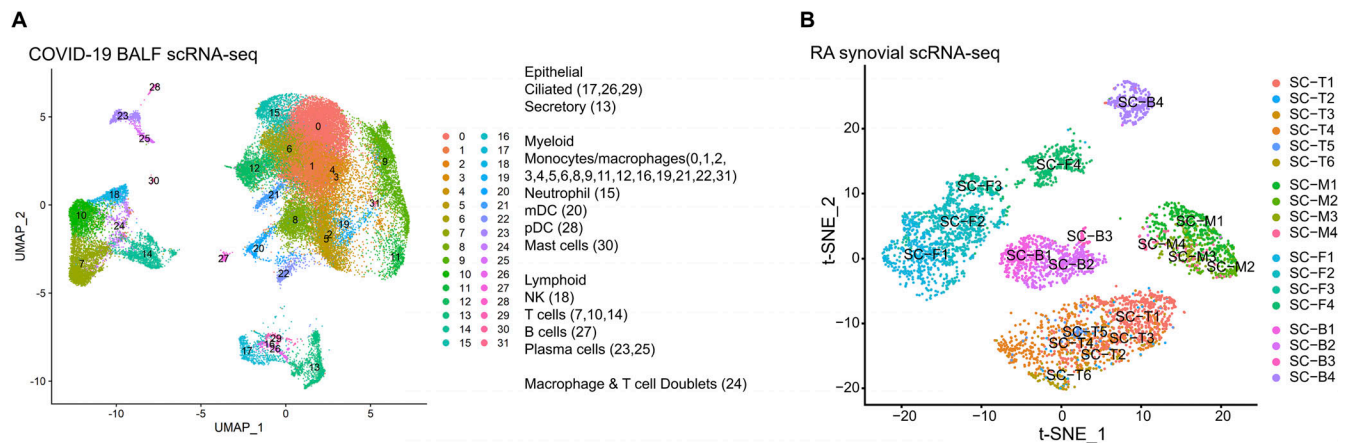
Figure S1.   **Clustering analyses of scRNA-seq datasets. (A)** UMAP projection of BALF cells from COVID-19 patients. Cell type annotations were labeled for each cluster. Monocyte/macrophage clusters (CD14^{high} CD68^{high}) were used for the subsequent analyses. **(B)** t-Distributed stochastic neighbor embedding (t-SNE) projection of synovial cells from RA patients. Cell type annotations were labeled for each cluster. T, M, F, and B represent T cell, monocytes, fibroblasts, and B cells, respectively. Monocyte clusters (CD14^{high}) were used for the subsequent analyses. mDC, myeloid dendritic cells; NK, natural killer cells; pDC, plasmacytoid dendritic cells.
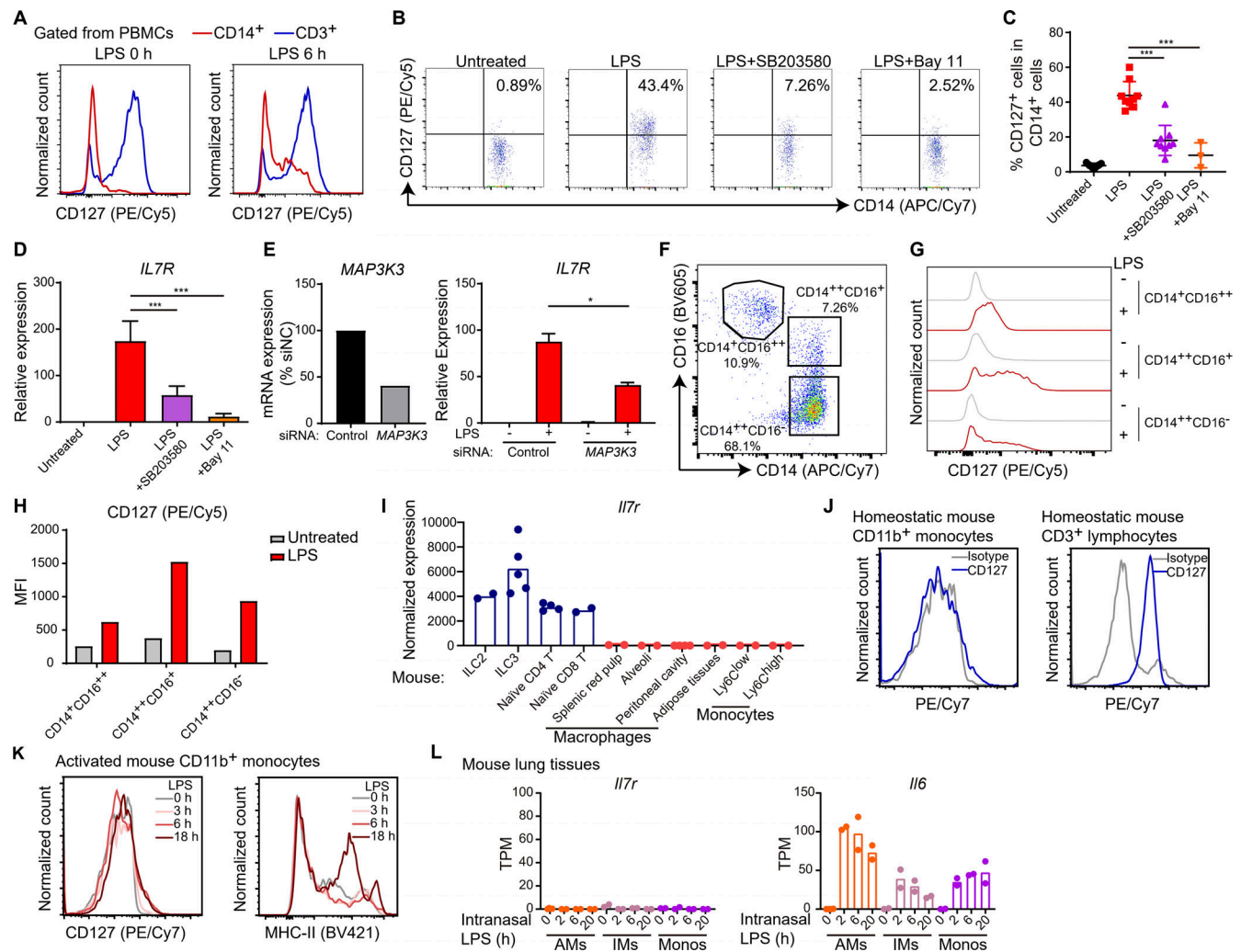
Figure S2. **Elicited CD127 expression represents a common but unique feature for activated human monocytes and is induced by TLR signaling.** **(A)** PBMCs from healthy donors were treated with or without 6-h LPS stimulation (10 ng/ml), and CD127 expression in CD3+ T cells and CD14+ monocytes was analyzed by FACS in each condition. Representative FACS distributions are shown from three independent experiments. **(B and C)** PBMCs form healthy donors were pretreated with DMSO or 10 µM SB203580 or 10 µM Bay 11-7082 (Bay 11) for 30 min and subsequently stimulated with or without 10 ng/ml LPS for 6 h as indicated. The protein levels of CD127 were measured by FACS and are shown as representative FACS distribution (B) and cumulative percentages (C) in CD14+ monocytes. ***, P < 0.001 by unpaired *t* test. Each data point represents an independent experiment. Data are shown as the mean ± SD of multiple independent experiments as listed, respectively: untreated *n* = 9, LPS *n* = 9, SB203580 *n* = 9, Bay 11-7082 *n* = 3. **(D)** CD14+ selected monocytes from healthy donors were pretreated with DMSO or 10 µM SB203580 or 10 µM Bay 11-7082 (Bay 11) for 30 min and subsequently stimulated with or without 10 ng/ml LPS for 6 h as indicated. mRNA of *IL7R* was measured by qPCR. The relative expression was normalized to internal control (*GAPDH*) and expressed relative to the untreated sample. ***, P < 0.001 by unpaired *t* test. Data are shown as the mean ± SD of multiple independent experiments as listed, respectively: untreated *n* = 9, LPS *n* = 9, SB203580 *n* = 6, Bay 11-7082 *n* = 3. **(E)** CD14+ monocytes were transfected with negative control or *MAP3K3*-specific siRNAs. 2 d after transfection, cells were stimulated with LPS (10 ng/ml) for 3 h. Knockdown efficiency of *MAP3K3* was examined, and mRNA induction of *IL7R* by LPS stimulation in siControl and si*MAP3K3* transfected cells was measured by qPCR. Relative expression was normalized to internal control (*GAPDH*) and expressed relative to LPS untreated siControl sample. *, P < 0.05 by paired *t* test. *IL7R* expression data are shown as the mean ± SD of three independent experiments. **(F–H)** Three human monocyte populations were gated by CD14 and CD16 expression in FACS analysis of healthy donor PBMCs as shown in F. CD127 expression in three human monocyte populations was analyzed in conditions with or without LPS stimulation for 6 h. Representative FACS distribution (G) and mean fluorescence intensity (MFI; H) for CD127 expression are shown from three independent experiments. **(I)** The normalized *Il7r* expression level assessed by RNA-seq was obtained from the ImmGen database, and expression levels in multiple mouse immune cell types are shown, including ILC2 and ILC3 in small intestines, naïve CD4 and CD8 T cells in spleens, macrophages across different tissues, and Ly6C delimited blood monocyte populations. Each data point represents each individual replicate sample included in the ImmGen database. **(J and K)** Mouse blood cells (red blood cells lysed) were treated with or without 100 ng/ml LPS for different time points as indicated. In the homeostatic condition, CD127 expression in mouse CD11b+ monocytes was analyzed by FACS, and expression in CD3+ lymphoid cells served as a positive control (J). Upon LPS stimulation, the expression of CD127 and MHC-II on mouse CD11b+ monocytes was analyzed by FACS (K). **(L)** The published RNA-seq datasets were generated in macrophages and monocytes isolated from mouse lung tissues, where mice were intranasally treated with 10 µg LPS per mouse for different time points. The expression levels (gene-specific transcripts per million total transcripts [TPMs]) of *Il7r* and *Il6* were assessed and are shown across alveolar macrophages (AMs), interstitial macrophages (IMs), and tissue monocytes (Monos). Each data point represents each independent biological replicate in the original datasets. Independent experiments in A–H were performed with cells from one healthy donor for each experiment.
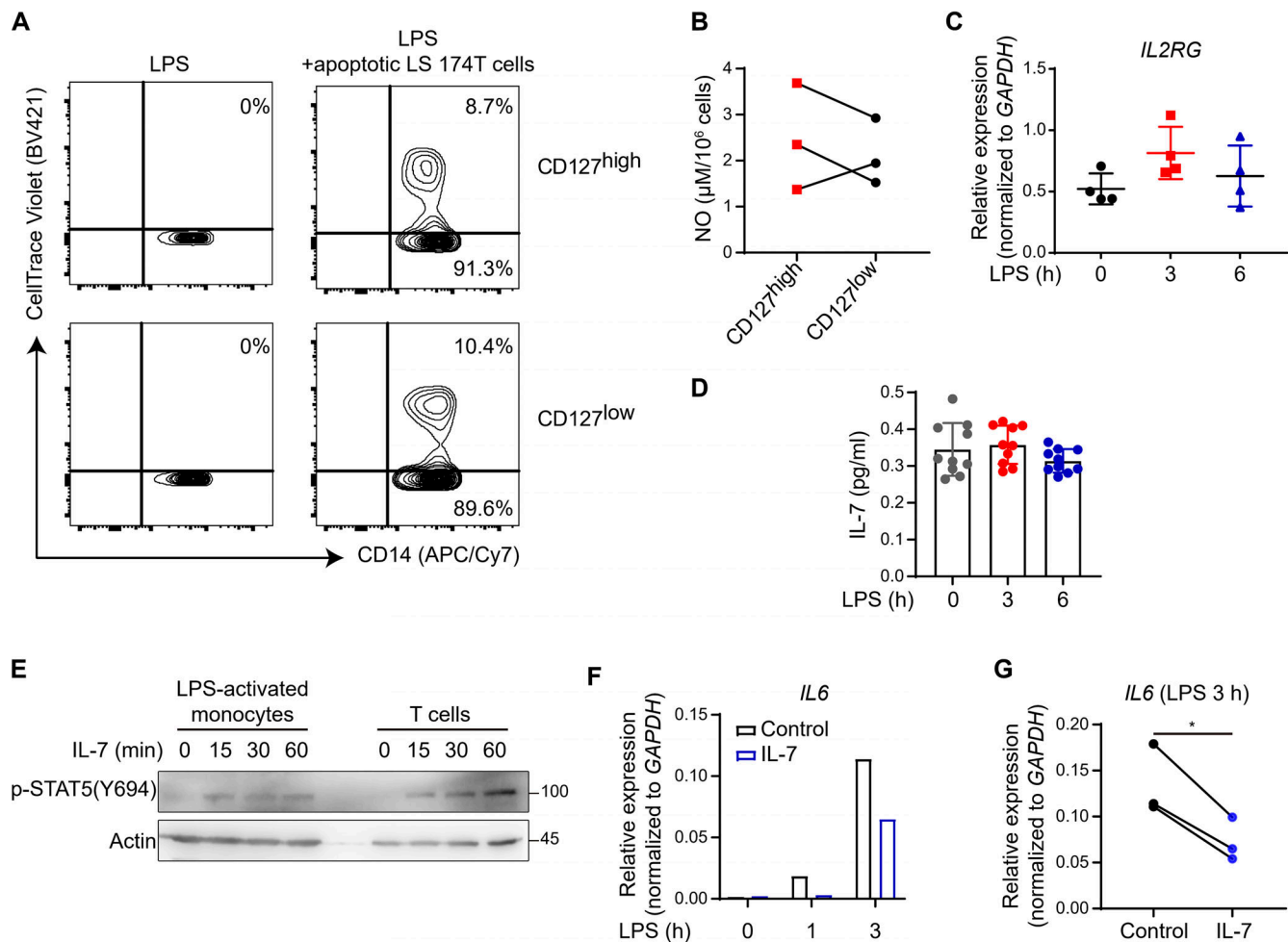
Figure S3. **Functional CD127–STAT5 axis imposes hypoinflammatory human monocyte phenotypes. (A)** CellTrace Violet–labeled human colonic epithelial cell line LS 174T cells were administered with H_2O_2 to induce apoptosis. Human CD14$^+$ monocytes were treated with 10 ng/ml LPS for 6 h and subsequently cocultured with apoptotic LS 174T cells for 1 h. Phagocytosed apoptotic cells were measured by CellTrace Violet (BV421) signals in CD127^{high} and CD127^{low} populations in CD14$^+$ monocytes. Representative FACS distribution is shown from three independent experiments. **(B)** NO production in FACS-sorted CD127^{high} and CD127^{low} populations from CD14$^+$ monocytes upon LPS stimulation for 6 h. NO production was measured and expressed as NO concentration in 100 µl cell lysis for 10^6 sorted cells. Each pair of data points represents an independent experiment. Results from three independent experiments are shown. **(C)** Human CD14$^+$ monocytes were treated with 10 ng/ml LPS for 3 h and 6 h, and the mRNA levels of *IL2RG* were measured by qPCR. Relative expression was normalized to *GAPDH* as an internal control. Each data point represents an independent experiment. Data are shown as the mean ± SD of four independent experiments. **(D)** IL-7 concentration in culture media of human monocytes upon LPS stimulation for the indicated times. Each data point represents an independent experiment. Data are shown as the mean ± SD of 10 independent experiments. **(E)** Human CD14$^+$ monocytes were pretreated with 10 ng/ml LPS for 6 h and subsequently stimulated with recombinant human IL-7 (10 ng/ml) for the indicated times. Meanwhile, CD3$^+$ T cells from the same donor were treated with 10 ng/ml IL-7 for the indicated times. The protein levels of p-STAT5(Y694) were detected by Western blotting. β-Actin was used as a loading control. **(F and G)** Human CD14$^+$ monocytes were activated by 1 ng/ml LPS with or without 100 pg/ml IL-7 simultaneous stimulation for the indicated time points. The mRNA levels of *IL6* were measured by qPCR. Relative expression was normalized to *GAPDH* as an internal control. One representative result from three independent experiments is shown in F. Statistical results of expression data upon 3-h indicated treatments from three independent experiments are shown in G. *, P < 0.05 by paired *t* test. Independent experiments in A–G were performed with cells from one healthy donor for each experiment.
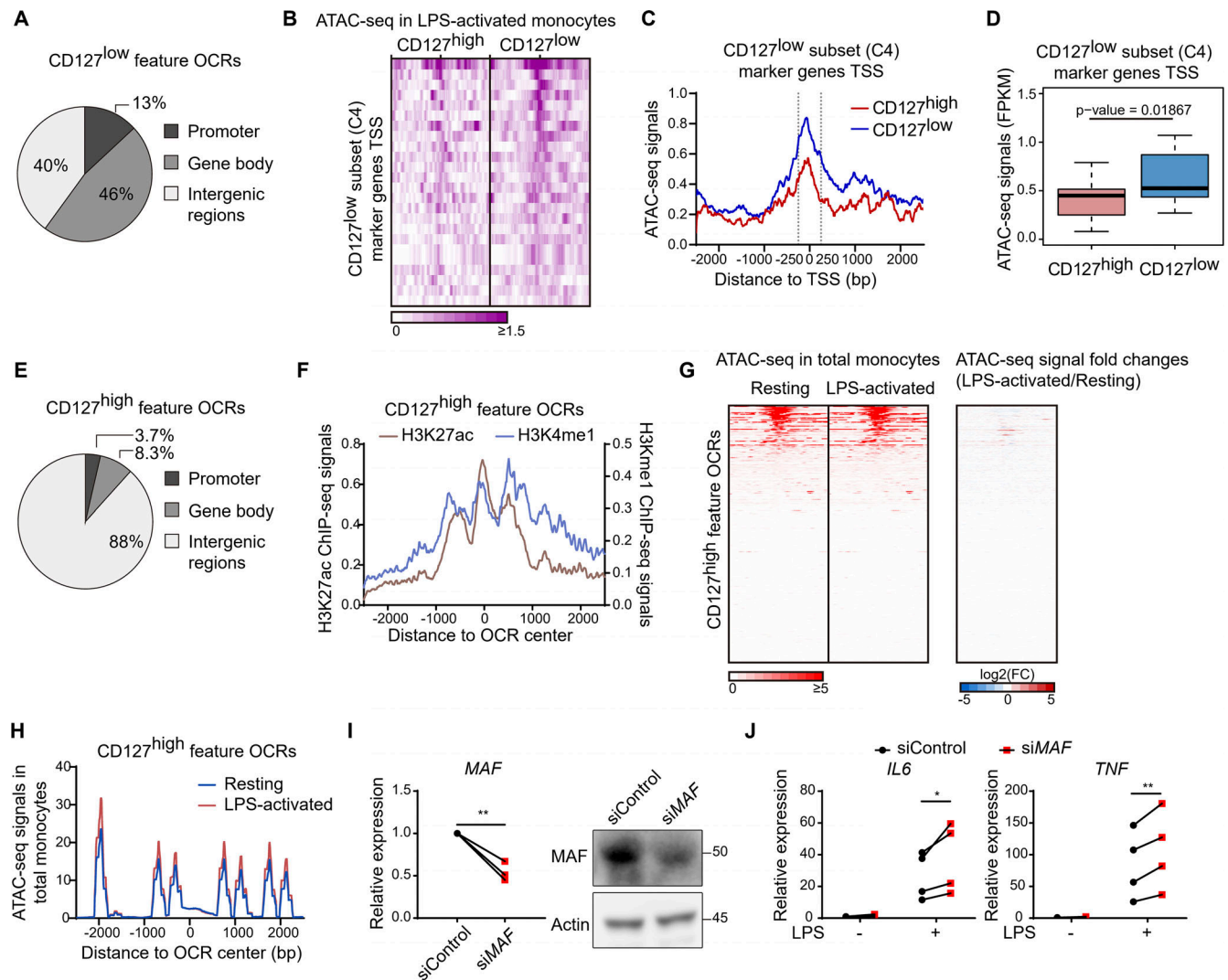
Figure S4. CD127 expression coordinates enhancer-like OCRs in CD127^high monocytes. (A) Pie graph shows the genomic distribution of CD127^low monocyte feature OCRs. **(B and C)** ATAC-seq signals in CD127^high monocytes and CD127^low monocytes are shown around TSSs (±2,500 bp) of marker genes for CD127^low subset (cluster 4) in Fig. 3 D. Heat map shows the ATAC-seq signals for individual TSS regions (B), and the average ATAC-seq signals are shown in a histogram (C). **(D)** ATAC-seq signals in CD127^high and CD127^low monocytes were counted around TSS regions (±250 bp) of marker genes for CD127^low subset (cluster 4) in Fig. 3 D. FPKM values are shown in box plot. P value was calculated by Wilcoxon rank-sum test. **(E)** Pie graph shows the genomic distribution of CD127^high monocyte feature OCRs. **(F)** Average ChIP-seq signals of H3K27ac and H3K4me1 in LPS-activated monocytes were assessed around CD127^high feature OCRs and expressed by different colors as indicated in the plot. **(G)** Heat maps (left) show the ATAC-seq signals around the CD127^high feature OCRs in human monocytes with or without LPS treatment for 4 h. The ATAC-seq signals were pooled from two independent experiments from the original datasets and were quantified every 10-bp bin from the centers of the each individual CD127^high feature OCR. The ATAC-seq signal fold changes (right) were shown as the value of $\log_2$-transformed LPS-activated/resting ratio for each bin and expressed by colors from blue (negative) to red (positive). **(H)** The average ATAC-seq signals around the CD127^high feature OCRs in human monocytes with or without LPS treatment for 4 h. **(I and J)** CD14^+ monocytes were transfected with negative control or *MAF*-specific siRNA (siControl or si*MAF*). 2 d after transfection, knockdown efficiency was assessed by measuring *MAF* mRNA with qPCR (relative expression is normalized to internal control (*GAPDH*) and expressed relative to siControl group) and MAF protein levels with immunoblotting (I). 2 d after transfection, cells were stimulated with LPS (10 ng/ml) for 3 h, and mRNA levels of *IL6* and *TNF* were measured by qPCR (J). Relative expression was normalized to internal control (*GAPDH*) and expressed relative to LPS untreated siControl sample. *, P < 0.05; **, P < 0.01; paired *t* test. Each pair of data points represents an independent experiment with cells from a healthy donor. The results from four independent experiments are shown.
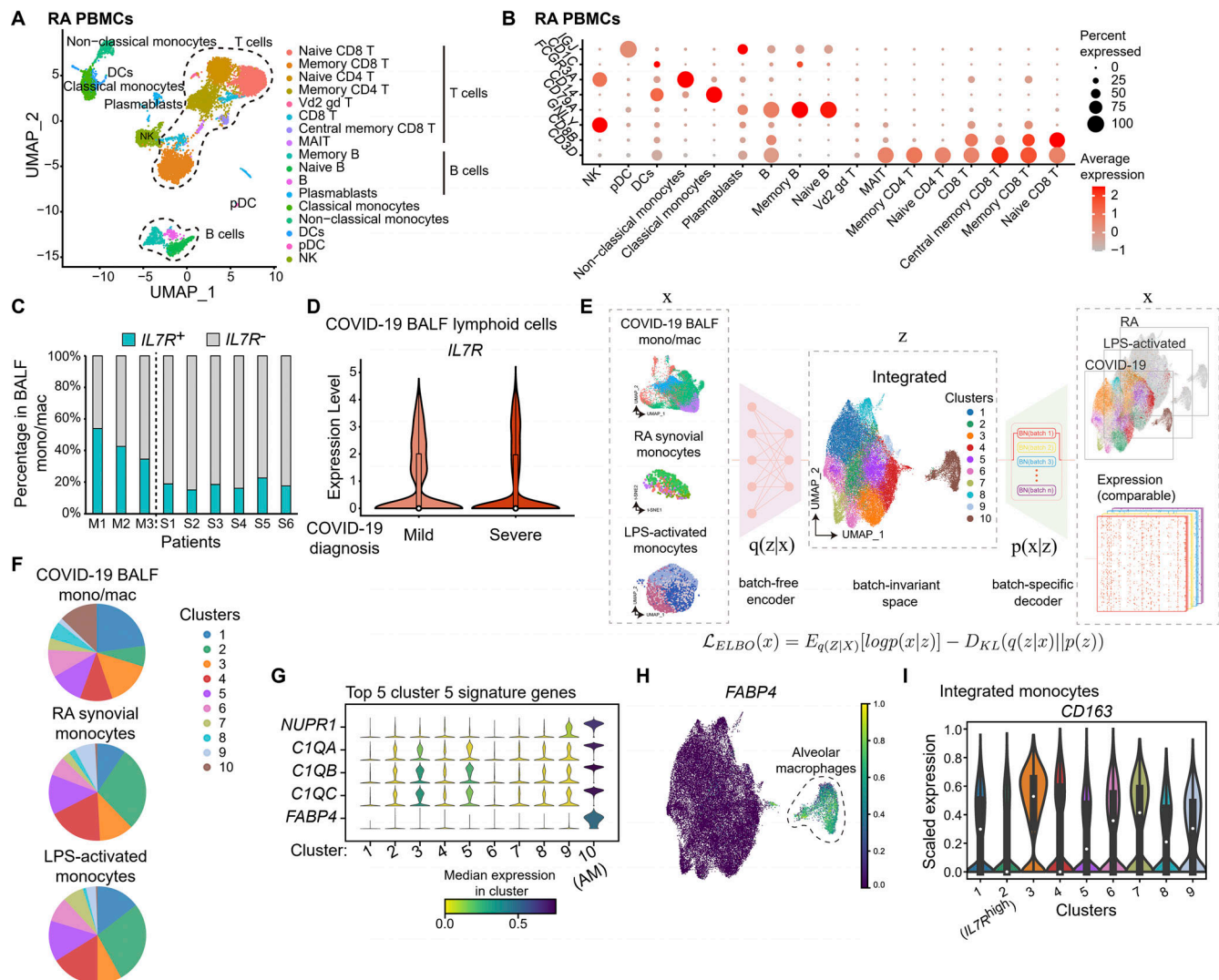
Figure S5. **CD127 expression designates a functionally distinct monocyte subset. (A)** UMAP projection of PBMCs from an RA patient. Cell type annotations were labeled for each cluster. DC, dendritic cell; pDC, plasmacytoid dendritic cell. **(B)** Heat map shows the expression of hallmark genes in different cell clusters from RA PBMCs. The scaled average expression levels of marker genes and the percentage of cells expressing marker genes are expressed by color and size of each dot corresponding to cell clusters, respectively. MAIT, mucosal associated invariant T cell; NK, natural killer cell. **(C)** The percentages of $IL7R^+$ cells in BALF monocytes/macrophages (mono/mac) from mild or severe COVID-19 patients are individually shown for each patient. **(D)** Lymphoid cells from COVID-19 patient BALF were subgrouped by the diagnosed disease severity. Violin plot shows the expression of $IL7R$ in BALF lymphoid cells from mild or severe COVID-19 patients. Each overlaid box indicates the interquartile range with the median shown as a circle. **(E)** The schematic plot briefly shows the methodology of SCALEX. The asymmetric variational autoencoder (VAE) framework was structured for SCALEX via a batch-free encoder and a batch-specific decoder, in which batch-free encoder extracted the batch-invariant biological features (z) that were masked by batch-related variations among the input scRNA-seq datasets (x), and batch-specific decoder incorporated the batch information when reconstructing the expression matrix for integrated data. Such a probabilistic model of SCALEX is shown in the panel and is briefly introduced in Materials and methods. On this basis, we integrated monocytes from COVID-19 BALF, RA synovial tissue, and LPS-treated monocytes by SCALEX to generate a comparable integrated scRNA-seq dataset with preservation of the biological features for each incorporated component. **(F)** Pie graphs projecting the percentage of each cluster in E in total monocytes or macrophages from different tissue sources. **(G)** The stacked violin plot shows the expression of the top five cluster 10 signature genes in all 10 clusters shown in E. Median expression levels for each gene in each cluster were indicated by colors. **(H)** UMAP projection of integrated monocytes/macrophages in E. $FABP4$ expression in cells was quantitatively visualized by the indicated colors. Cells corresponding to cluster 10 were highlighted by a dotted line as alveolar macrophages, given the specific $FABP4$ expression pattern. **(I)** Violin plot shows the expression of $CD163$ among nine clusters of integrated monocytes in Fig. 6 G, in which cluster 2 was designated as the $IL7R^{high}$ cluster. Each overlaid box indicates the interquartile range with the median shown as a circle.